



TECHNISCHE  
UNIVERSITÄT  
WIEN  
Vienna University of Technology

## **Diplomarbeit**

# **Comparison of the aging behavior in industrial and laboratory-made pure aluminium 6xxx-series alloys**

Ausgeführt zum Zwecke der Erlangung des akademischen Grades eines Diplom-  
Ingenieurs unter der Leitung von

**Univ. Prof. Dipl.-Ing. Dr. tech. Ernst Kozeschnik**

und

**Dipl.-Ing. Dr. tech. Ahmad Falahati**

E308

Institut für Werkstoffwissenschaften und Werkstofftechnologie

Eingereicht an der Technischen Universität Wien

**Fakultät für Maschinenwesen und Betriebswissenschaften**

von

**Thomas Weisz, BSc**

0725273

Laxenburgerstraße 127/2/1/4

1100 Wien

Wien, im April 2014

---

Unterschrift

## Abstract

The microstructure evolution of two different aluminium 6xxx-series was investigated during artificial aging. One alloy is a laboratory-made pure 6xxx alloy, representing a ternary system only including aluminium, magnesium and silicon. The second alloy is an industrial manufactured aluminium A6016 alloy, with the same main chemical composition as pure laboratory-made alloy which includes several accompanying elements (e.g. Fe, Ti, Mn, Cu). The behavior of these two alloys during artificial aging was investigated in detail via light microscopy, differential scanning calorimetry (DSC), hardness measurements and transmission electron microscopy (TEM).

Grain size of both materials is highly different because of the lack of grain-refining elements in the ternary alloy. The laboratory-made pure alloy showed slight lower kinetics during DSC run compared to the industrial alloy. The hardness evolution during the industrial aging heat treatment showed slightly higher hardness in T4 condition for the industrial alloy, which is a result of smaller grains and higher number of dispersoid phases. This difference in hardness remains constant throughout the industrial aging heat treatment. The hardness of the laboratory-made alloy shows slight increase at the end of the aging treatment which was not expected. The reason must be the subject of further investigations. TEM investigations showed a higher amount of dispersoids in the industrial alloy. During the industrial aging treatment precipitation of  $\beta''$  was detected in both alloys. The number density of the laboratory-made alloy was one order of magnitude lower than those of the industrial AA6016, but the precipitates showed almost the same size.

The hardness development by artificial aging process was not affected significantly by the absence of accompanying elements. Main differences of both alloys are the smaller grain size, higher number of dispersoids and slightly faster precipitation-kinetics in the industrial alloy.

## Kurzfassung

Die Mikrostruktur von zwei unterschiedlichen Aluminium 6xxx-Legierungen während des Aushärtens wurde untersucht. Die erste Legierung wurde im Labor hergestellt und stellt ein ternäres System dar, welches nur die Hauptlegierungselemente Aluminium, Magnesium und Silizium enthält. Bei dem zweiten zu untersuchenden Material handelt es sich um ein industriell hergestellte AA6061 Legierung, welche die gleiche chemische Zusammensetzung hinsichtlich der Hauptlegierungselemente besitzt, allerdings auch weitere Begleitlegierungselemente wie Eisen, Titan, Mangan und Kupfer enthält. Das Verhalten dieser beiden Legierungen während des Aushärtens wurde mittels Lichtmikroskop, Differential Scanning Calorimetry (DSC), Härtemessungen und Transmissionselektronenmikroskopie (TEM) untersucht.

Die Korngröße der beiden Materialien unterscheidet sich aufgrund der fehlenden kornfeinenden Elemente im ternären System wesentlich vom industriellen Material. Die Reinlegierung zeigte außerdem eine leicht verzögerte Ausscheidungskinetik während der DSC-Untersuchungen. Die Entwicklung der Härte während einer industriellen Wärmebehandlung zeigte eine leicht erhöhte Festigkeit des industriellen Materials im Zustand T4, was mit einer geringeren Korngröße und einer höheren Anzahl an Dispersoiden begründet wird. Dieser Unterschied bleibt während des industriellen Härtungsprozesses annähernd konstant. Lediglich am Ende zeigt die im Labor hergestellte Probe einen unerwarteten geringen Anstieg der Härte. Dieser Effekt muss mittels weiterer Versuche untersucht werden, um eine Erklärung für dieses Phänomen zu finden. Die TEM Untersuchungen zeigten eine Höhere Anzahl von Dispersoiden in der industriellen Legierung. Während des industriellen Aushärtungsprozesses wurden in beiden Legierungen  $\beta''$  Ausscheidungen beobachtet. Deren Teilchendichte ist in der Reinlegierung um eine Größenordnung geringer als jene des industriellen Materials, wobei die Ausscheidungen beinahe dieselbe Größe aufweisen.

Der industrielle Aushärtungsprozess wird durch die Begleitelemente nicht wesentlich beeinflusst. Der größte Unterschied liegt in der geringeren Korngröße, der höheren Zahl an Dispersoiden, sowie in der geringfügig schnelleren Ausscheidungskinetik der industriellen AA6016 Legierung.

## Acknowledgements

At first I would like to thank Prof. Kozeschnik and Dr. Falahati for giving me the opportunity to expand my knowledge in the field of materials science and technology and giving me a very pleasant welcome at the institute. They were very patient throughout this time and supported me in many different ways.

Financial support by the Austrian Federal Government (in particular from Bundesministerium für Verkehr, Innovation und Technologie and Bundesministerium für Wirtschaft, Familie und Jugend) represented by Österreichische Forschungsförderungsgesellschaft mbH and the Styrian and the Tyrolean Provincial Government, represented by Steirische Wirtschaftsförderungsgesellschaft mbH and Standortagentur Tirol, within the framework of the COMET Funding Programme is gratefully acknowledged.

I would like to thank Peter Lang, who aroused my interest in the field of aluminium alloys, for sharing his knowledge with me. A special thank is given to Tomasz Wojcik, who helped me in terms of sample preparation and TEM investigations. Without him a main part of this work would not exist. Erwin Povoden-Karadeniz is highly acknowledged for sharing his knowledge about precipitation sequence and thermodynamic assessment. I also have to thank Heinz Kaminski, Edith Asiemo and Christian Zaruba for supporting me in the laboratory.

I like to thank my colleagues Georg Stechauner, Martin Lückl, Siamak Rafiezadeh and Simon Großeiber for the support and small hints they gave, but also for the relaxing time I had with them offside the working hours.

I appreciate the help of Alice Redermayer, Christian Steinkellner, Michael Kainz and Astrid Weisz for proofreading this thesis.

I have to thank my parents for supporting me in so many ways throughout my studies. Without them none of this would have been possible.

Finally, I would like to thank Patricia who supported and encouraged me to reach my goals, especially during rough times.

# Table of contents

1	Introduction .....	1
2	Objectives .....	3
3	State of the art .....	4
3.1	The production process of Al-6xxx series alloys.....	4
3.2	Direct Chill (DC) casting .....	5
3.2.1	Parameters influencing the grain structure .....	6
3.2.2	Primary phases .....	8
3.3	Homogenization .....	10
3.4	Hot rolling .....	11
3.5	Solution heat treatment and quenching .....	12
3.6	Aging of Al-6xxx series alloys.....	13
3.6.1	Influence of vacancies and natural aging.....	14
3.6.2	The precipitation sequence in Al-Mg-Si alloys .....	15
3.6.3	Differential Scanning Calorimetry in Al-6xxx series alloys .....	17
3.6.4	Homogeneous and heterogeneous nucleation .....	19
3.6.5	Impact of precipitates on strength – precipitation hardening.....	22
4	Experimental.....	26
4.1	Used material .....	26
4.2	Metallography .....	27
4.3	DSC measurements .....	28
4.4	Hardness measurements .....	29
4.5	TEM investigations .....	31
5	Results.....	32
5.1	Metallography.....	32
5.2	DSC measurements .....	32
5.3	Hardness measurements .....	34

---

5.4	TEM investigations .....	35
5.4.1	TEM - condition 1 .....	35
5.4.2	TEM – condition 2 .....	38
5.4.3	TEM – condition 3 .....	40
5.4.4	Evolution of precipitate size and number density .....	41
6	Discussion.....	43
6.1	Metallography .....	43
6.2	Comparison of the precipitation kinetics .....	43
6.3	Differences in the Hardness evolution during industrial heat treatment.....	45
6.4	Comparison of TEM-results.....	46
7	Summary and Conclusion .....	49
8	References.....	51
9	List of figures.....	54

# 1 Introduction

In times, where ecological and consequently financial issues in industry become more and more important, improvements in the material sector are a practical way to face these challenges. The increasing use of light-weight materials in the automotive segment of industry is a prominent example for this trend of business. One class of alloys that is widely used today are aluminium alloys. The existence of the element aluminium was firstly postulated around 1807 by the British scientist Sir Humphrey Davy. Throughout the next decades of the 19th century this element was investigated in more and more detail and is nowadays one of the most important construction materials in the industry. This had only become possible due to the invention of aluminium alloys, because the physical properties of pure aluminium cannot face many of the challenges given by industrial applications. Especially the low hardness- and toughness values of pure aluminium are limiting its use as construction material. By addition of several alloying elements, a large variety of alloys for many different applications can be produced. Aluminium alloys can be classified in casting and wrought alloys. Main difference are the amount of alloying elements and a different production process. This work deals with aluminum wrought alloys which can be classified further by chemical composition. The classification of aluminium wrought alloys is shown below:

- 1xxx aluminium of 99% min. purity
- 2xxx aluminium and copper alloys
- 3xxx aluminium and manganese alloys
- 4xxx aluminium and silicon alloys
- 5xxx aluminium and magnesium alloys
- 6xxx aluminium, Mg and Si alloys
- 7xxx aluminium, Zn and Mg alloys
- 8xxx other alloys (e.g. aluminium lithium)

The 1xxx, 3xxx and 8xxx-series alloys gain their strength by work hardening, while alloys which are part of the 2xxx, 6xxx, 7xxx and 8xxx-series are heat treatable and reach their strength mainly by precipitation hardening.

This thesis deals with alloys out of the 6xxx-series, which have magnesium and silicon as main alloying elements. In addition to these elements, many accompanying elements are also present in industrial alloys, to improve several

---

properties. One element is titanium, which is used as grain refiner. Other accompanying elements are iron, manganese, chromium and copper, which form dispersoids in the material, that affect the recrystallization behavior and contribute a little to the strength of the material. This work shows the effects of these alloying elements by comparing an industrial alloy with a laboratory-made pure ternary system, which contains only the main alloying elements aluminium, magnesium and silicon. The investigations mainly focus on these effects during an industrial heat treatment used for artificial aging.



---

## 2 Objectives

This thesis focuses on a laboratory-made pure aluminium alloy with a composition 0.39wt% Mg, 1.07wt% Si and rest Al, which is very similar to an industrial AA6016 wrought alloy. The age-hardenable 6xxx-series alloys are mainly used in the automotive industry. The difference between the laboratory and industrial material is the presence of additional accompanying elements. One element, which is present in nearly every commercial Al-Mg-Si alloys, is iron. It is originated from the production of primary and secondary aluminium, but can also be added on purpose. Elements such as chromium, titanium, scandium or zinc are also added to the alloy to improve several properties of the material. Titanium for instance is used to reduce grain size and to increase recrystallization-resistance. As already mentioned, the 6xxx-series alloys are age-hardenable and can be heat treated to improve their strength. During the aging heat treatment precipitates are built in a specific precipitation sequence.

It is the aim of this work to show the effect of absence of accompanying elements on the microstructure evolution of the material in compare to industrial material. The precipitation kinetic of both materials is compared with each other via differential scanning calorimetry (DSC). The precipitate-parameters such as number density, size and phase fraction and hardness are compared during an industrial aging process.

Investigations are performed via DSC, transmission electron microscopy (TEM) and hardness measurements.

### 3 State of the art

This section gives an introduction into the production steps of Al-6xxx series alloys. Based on these steps the evolution of the microstructure is explained in detail. The precipitation sequence of the alloy which occurs during the artificial-aging process will be reviewed briefly. For a deeper understanding of the ongoing processes within the material the basics of nucleation theory are explained shortly.

#### 3.1 The production process of Al-6xxx series alloys

The schematic production process of Al-6xxx series alloys is shown Figure 1. The production starts with a Direct Chill (DC)-casting step followed by homogenization.

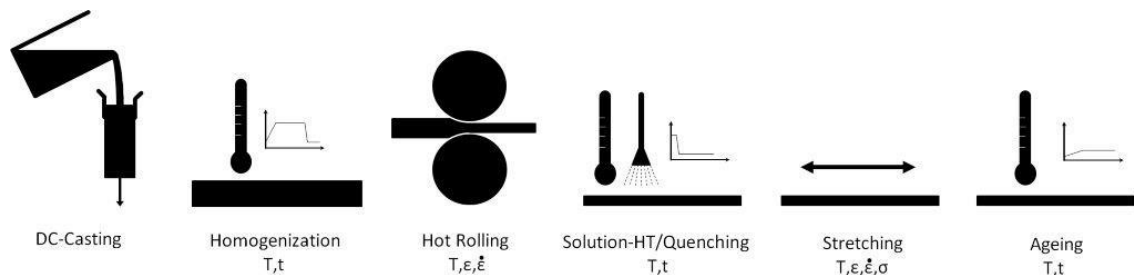


**Figure 1: Process-steps in the production of 6xxx-series alloys.**

In case of 6xxx- series alloys the heat which is brought into the material during this step is also used to provide the correct temperature for hot rolling. During the hot rolling the material is deformed to its final thickness. In some cases this step is followed by cold rolling for higher accuracy concerning the dimensions. During the solution heat treatment the sheets or plates are exposed to a specific elevated temperature for an appropriate period of time. By rapid quenching (e.g. water-quenching) a supersaturated solid solution is formed, which is a requirement for the formation of precipitates during aging. Quenching also induces high thermal-stresses in the product, which lead to plastic deformation. Because this is not acceptable in terms of product quality, the plates must be straightened by stretching to a slight plastic deformation. This step is not described in this work in detail, because it was not performed during sample preparation. It should be kept in mind that this step can have an effect on age

hardening due to creation of a high number of dislocations in the material. To reach the desired strength of the alloy, it is aged artificially during a specific heat treatment. This leads to precipitation of finely dispersed particles that act as barrier for dislocation movement and thereby improve the strength of the material. In the following sections of this thesis, the microstructure evolution in each production step of these alloys is discussed and special attention is paid to the accompanying elements and their influence on the microstructure.

### 3.2 Direct Chill (DC) casting

As in most production-sequences of widely industrial-used metallic materials, the production of aluminium alloys starts with melting and setting up the correct chemical composition of the alloy. The melt is then cast in a variety of casting technologies. One of the most commonly used technologies is Direct Chill (DC) [1] casting. The basic principle is shown in Figure 2.

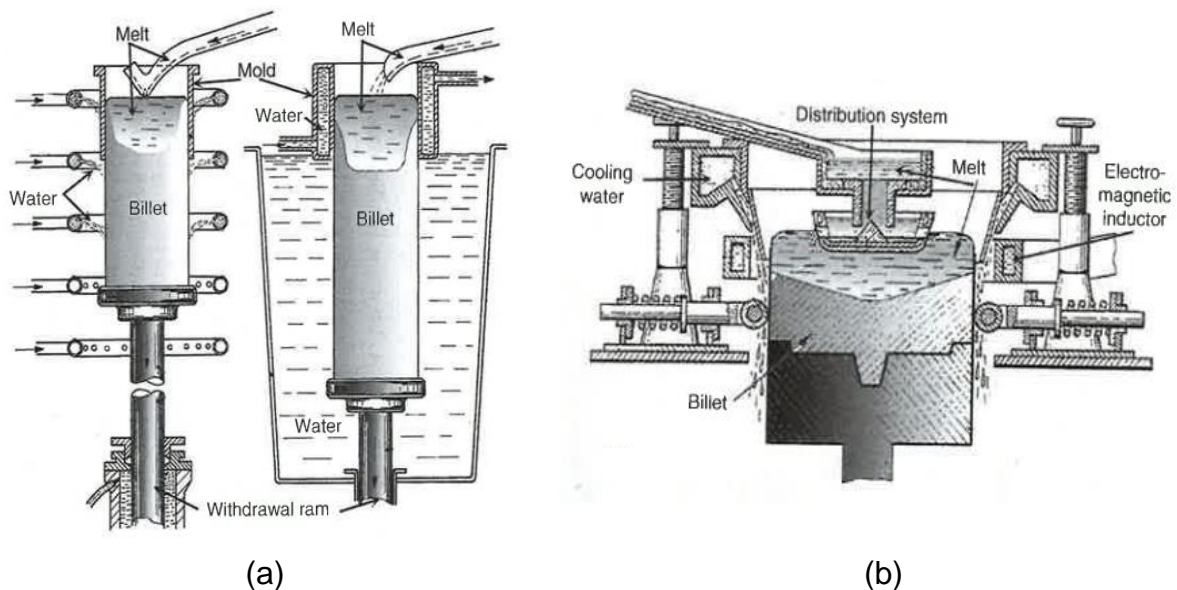


**Figure 2: DC casting methods; early methods (a), modern electromagnetic casting (b) [1].**

The advantage of the technology lies in the quiet low height of the mold. As the process is started the withdrawal ram is positioned right below the mold. As the liquid material solidifies at the water-cooled mold walls and the ram, a solid billet is produced. In accordance to the solidification velocity, the ram is moved downwards to allow the billet to grow. As a consequence of solidification and cooling, the volume of the billet decreases causing a gap between mold and billet. This gap often causes problems, because the quite unstable hot material

is not supported by the mold walls and therefore leads to an uneven surface of the billet. This problem was solved by the introduction of a moldless DC casting method, using a strong electromagnetic field to hold the billet in position. The scheme of this technology is shown in Figure 2(b).

### 3.2.1 Parameters influencing the grain structure

Cooling rate and the melt temperature influence the microstructure of the alloy during casting. Especially the grain size of the material is governed by these parameters. In most applications of aluminium alloys, a small grain size is required to achieve a high contribution to strength and ductility. Also a better surface quality is produced [2]. The effect of cooling rate on the grain size and dendrite arm spacing is shown in Figure 3.

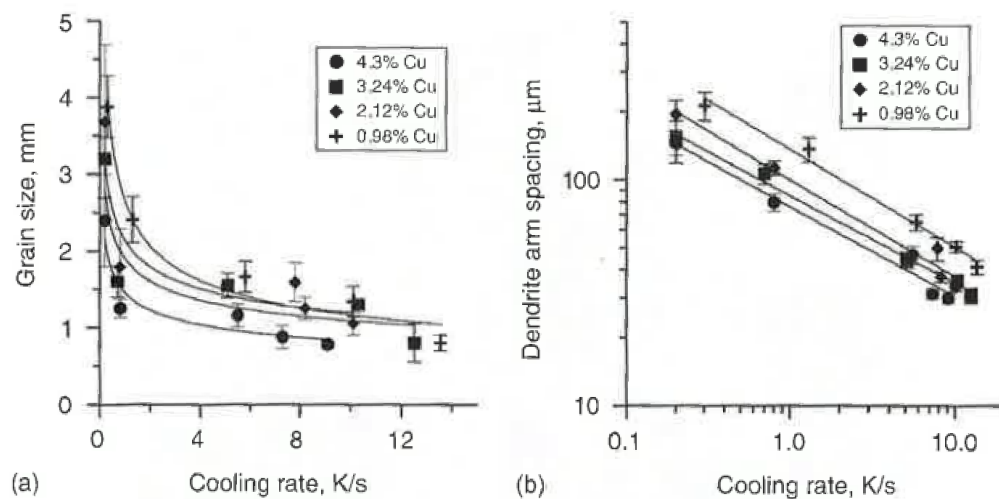


**Figure 3: Effect of cooling rate on grain size (a) and dendrite arm spacing (b) of Al-Cu alloys [1].**

The grain size and the dendrite arm spacing of emerging dendrites significantly decrease with increasing cooling rate. Figure 3 shows the effect of alloy content, which is rather small in case of Al-Cu systems.

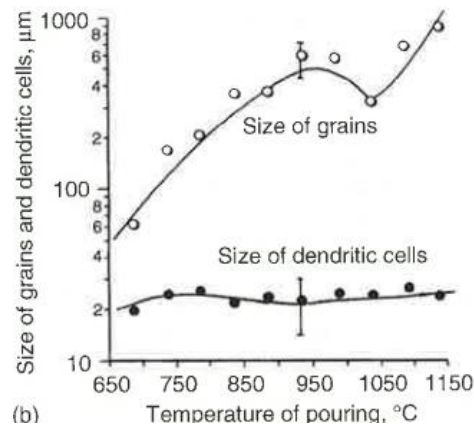


**Figure 4: Influence of melt temperature on cast structure of an AA2024 alloy [1].**

The melt temperature during the cast affects the grain size and dendritic arm spacing. As an example, Figure 4 shows this influence in an AA2024 alloy. The grain size increases until a specific temperature is reached. This is followed by a slight decrease and then the grains coarsen again with rising temperature while the size of the dendrites remains nearly constant with temperature. This is not the case for pure aluminium, where the grain size remains decreasing after a specific point and the size of the dendritic cells is not constant with temperature.

The mentioned parameters are not the only way to reach a specific grain structure. A very common possibility is the addition of small amounts of transition elements which build a high number and fine distribution of nuclei for solidification.

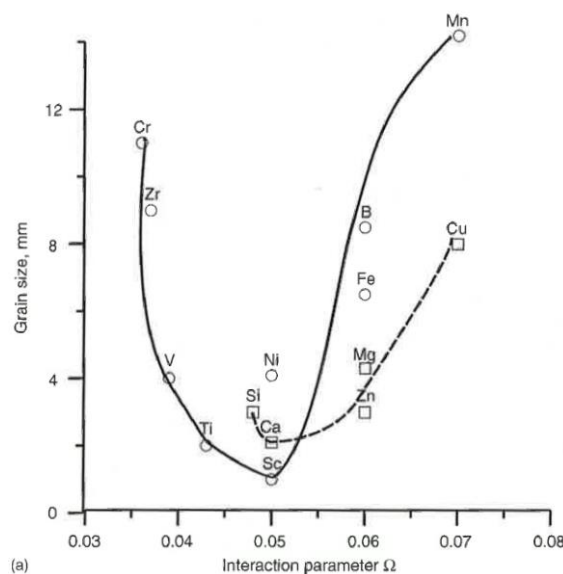


**Figure 5: Influence of accompanying elements on grain size of as-cast Al-alloys [1].**

Figure 5 shows the influence on the grain size by different alloying elements, where the grain size is plotted over the interaction parameter  $\Omega$  that is based on atomic structure of the transition element and the aluminium matrix. The solid line represents elements of the so called nucleation-type and the dashed line represents elements of the surface-active-type grain refiners. Nucleation-type elements have small structural mismatch between the substrate and aluminium. Those of surface-active-type lower the interfacial energy between substrate and aluminium and therefore facilitate nucleation. As can be seen titanium and scandium show the best values for grain refinement. In industry, mainly titanium in combination with e.g. B, C and Zr is used, because of the rather high costs for scandium. Not only these special transition elements have an effect on grain size, also other accompanying elements such as manganese, chromium and iron act as grain refiners due to their ability to form finely dispersed dispersoids [3].

### 3.2.2 Primary phases

From a metallographic point of view, the solidification of pure Al-Mg-Si is rather simple. In the solid state only the eutectic  $\text{Mg}_2\text{Si}$  phase is present besides aluminium. This is shown in Figure 6.

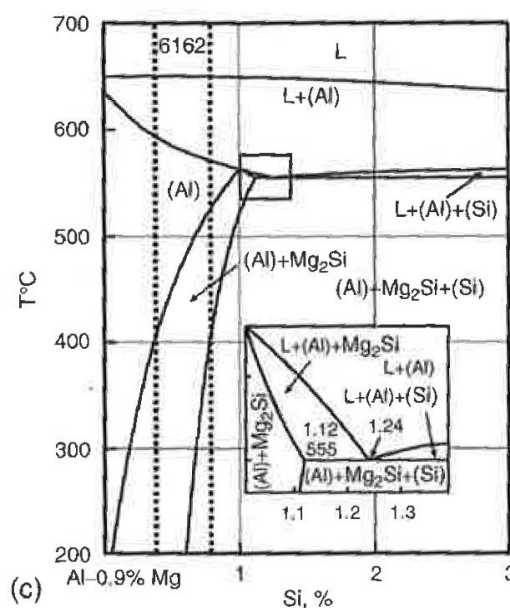


Figure 6: Phase diagram of an Al-Mg-Si alloy containing 0.9% magnesium [1].

Beside elements for grain refinement other accompanying elements are present in commercial aluminium alloys. One major element is iron, which results from

the production of primary aluminium where it is part in the bauxite. As noted before, the solidification of pure ternary Al-Mg-Si is quiet simple compared to industrial materials. In case of commercial Al-6xxx series alloys where iron and accompanying elements are part of chemical composition, several other phases can be part of the system. Based on the Mg/Si-ratio, specific phases are formed preferentially. In most cases the primary phases  $\text{Al}_3\text{Fe}$ ,  $\text{Al}_6\text{Fe}$ ,  $\alpha(\text{Al}_8\text{Fe}_2\text{Si})$ ,  $\beta(\text{Al}_5\text{FeSi})$  and  $\pi(\text{Al}_8\text{FeMg}_3\text{Si}_6)$  occur, where  $\text{Al}_3\text{Fe}$  is preferred at high Mg/Si-ratios and  $\beta(\text{Al}_5\text{FeSi})$  and  $\pi$  are favorable in the inverse case. However, also the  $\alpha$ -phase is built, because of its energetically advantageous morphology. Together with Fe, elements such as manganese and chromium are added which form phases  $\text{AlFeMnSi}$  or  $\text{AlCrFeMnSi}$  [4]. In some 6xxx alloys where copper is added, also copper containing phases can be present.

**Table 1: Properties of primary phases in Al-6xxx series alloys containing Fe, Cr and Mn [4].**

Notation	stoichiometry	Bravais lattice/ Space group	Lattice parameters and space group	Density ( $\delta$ ) $\text{kg/m}^3$
$\beta$	$\text{Al}_{4.5}\text{FeSi}$ [14], $\text{Al}_5\text{FeSi}$ [12]	Monoclinic	$a = 6.12 \text{ \AA}$ $b = 6.12 \text{ \AA}$ $c = 41.5 \text{ \AA}$ $\beta = 91^\circ$	3300-3350
$\alpha_b$ ( $\alpha'$ )	$\text{Al}_8\text{Fe}_2\text{Si}$	Hexagonal/ $P6_3$	$a = b = 12.3 \text{ \AA}$ $c = 26.2 \text{ \AA}$	3580
$\alpha_c$	(Fe containing) $\text{Al}_{12}\text{Fe}_3\text{Si}$ [19], $\text{Al}_{12-15}\text{Fe}_3\text{Si}_{1-2}$ [23]	Cubic $/Im_3$	$a = 12.56 \text{ \AA}$	3640
	(Fe+Mn containing) $\text{Al}_{12}(\text{FeMn})_3\text{Si}$ [24], $\text{Al}_{15}(\text{FeMn})_3\text{Si}_2$ [12]	Cubic/ $Im_3\text{-}Pm_3$	$a = 12.56\text{-}12.68 \text{ \AA}$	3640-3630
	(Mn containing) $\text{Al}_{12}\text{Mn}_3\text{Si}$ [24], $\text{Al}_{15}\text{Mn}_3\text{Si}_2$ [12], $\text{Al}_9\text{Mn}_2\text{Si}$ [22]	Cubic $/Pm_3$	$a = 12.68 \text{ \AA}$	3630

Typical primary phases and their stoichiometry, crystallographic structure, their lattice parameters and density in Al-Mg-Si alloys are shown in Table 1

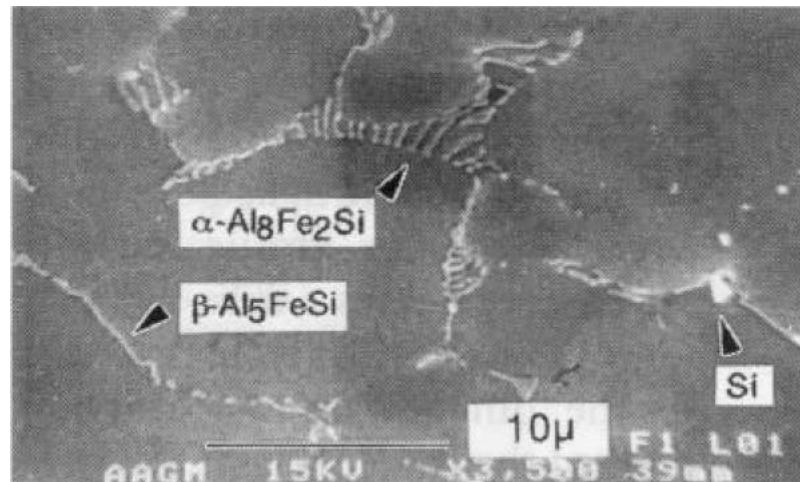


Figure 7: SEM of primary  $\alpha$  and  $\beta$  phases in an Al-Fe-Si alloy containing also Cu and Mn [5].

An example of a scanning electron microscope (SEM)-micrograph of  $\alpha$  and  $\beta$  phases in an as-cast Al-Mg-Si alloy is shown in Figure 7. The  $\alpha$ ( $\text{Al}_8\text{Fe}_2\text{Si}$ ) shows a chinese script like morphology, while the  $\beta$ ( $\text{Al}_5\text{FeSi}$ ) phase forms plate like [5].

### 3.3 Homogenization

After solidification, the microstructure of the material is inhomogeneous and hence unfavorable for further processing. The main problem is the low formability, which is caused by following facts [6]:

- Microsegregation, grain boundary segregation, low melting point eutectics and brittle intermetallic compounds
- Producing finely dispersed precipitates (dispersoids) for grain size control during rolling or extrusion.

It is the goal of this step to homogenize the microstructure in means of dissolving micro-segregation and also dissolving soluble primary phases. Especially the transformation of plate-like  $\beta$ ( $\text{Al}_5\text{FeSi}$ ) into spherical  $\alpha$ ( $\text{Al}_8\text{Fe}_2\text{Si}$ ) which has an advantageous effect and improves the formability of the alloy [6],[7].



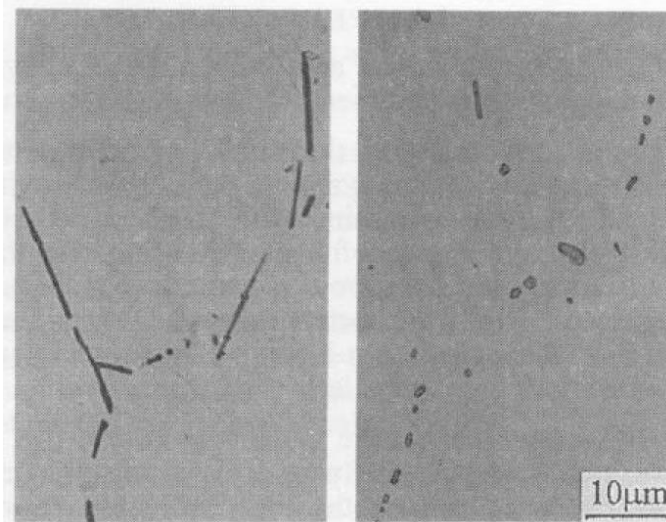


**Figure 8:  $\beta$  to  $\alpha$  transformation in AA6063 during homogenization at 565°C for 6h [7].**

This transformation is shown in Figure 8. Another very important reason for homogenization is the formation of secondary particles, or dispersoids, which control the recovery, recrystallization and grain growth of the alloy [8]. Dispersoids also contribute to the strength of the material by means of pinning dislocations during dislocation-movement. Homogenization of aluminium 6xxx-series alloys is performed at elevated temperatures around 540°C and higher in several temperature-sequences which depend on the chemical composition, microstructure and geometry of ingots. Based on these parameters the whole homogenization-process lasts approximately 12h to 24h.

### 3.4 Hot rolling

In case of 6xxx series alloys, the heat which is brought into the material during homogenization is directly used for hot rolling. Main purpose of this step is the reduction of thickness to the final geometry and also the breakdown of the cast structure to obtain good mechanical properties and also a high surface quality of sheets or plates. First, the ingot is processed in the brake down mill to break down large intermetallic phases containing iron and silicon. The material is recrystallized during this process and the primary phases are broken up to spherical shape [9]. This transforms the brittle cast structure in a ductile wrought alloy and closes also present voids and pores [10]. If necessary, this step is followed by tandem hot rolling where the thickness is further decreased by several passes.

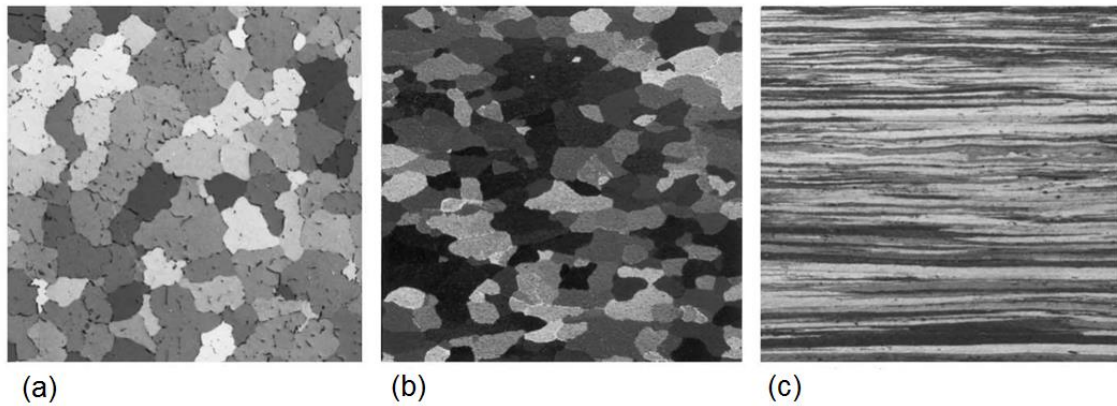


**Figure 9: Grain structure of AA6016 after casting and homogenization (a), homogenization and break-down mill (b) and after tandem hot rolling (c) [9].**

Figure 9 shows the microstructure of an AA6016 alloy after casting and homogenization (a), break-down rolling (b) and several hot rolling passes (c). The microsegregations which are visible in Figure 9a, are completely dissolved and the microstructure is slightly recrystallized (Figure 9b). Due to the high deformation, this structure is stretched and results in highly elongated grains (Figure 9c). The parameters temperature, strain, strain rate and inter-stand time control the final microstructure after hot rolling. In some cases hot rolling is followed by cold rolling to improve the surface quality or to increase the strength of the material by increasing the dislocation density. This is also necessary during the production of foils with very low thickness.

### 3.5 Solution heat treatment and quenching

Heat treatable aluminium wrought alloys reach their strength due to precipitation hardening. To enable such hardening effects, two major requirements must be fulfilled. First, the precipitating elements must be highly soluble at elevated temperatures. Secondly, the solubility must decrease significantly with decreasing temperature. In case of Al-6xxx series alloys the solution heat treatment is performed around 510°C to 550°C for approximately half an hour, which can be seen for instance in standard AMS2772F (2011). These values depend on the alloying content and geometry. During this solution heat treatment magnesium and silicon is solved and finely dispersed in the aluminium matrix. This silicon and magnesium is mainly taken from dissolving  $\text{Mg}_2\text{Si}$  phases but can also be originated from primary and secondary phases e.g.  $\alpha(\text{Al}_8\text{Fe}_2\text{Si})$  and other intermetallic phases and dispersoids containing

silicon and magnesium which were built during the previous process steps. Latter is the case when applying high temperatures and long process times, because these phases are much more stable. The dissolution of these phases and dispersoids is not favorable, since they have a positive effect on recrystallization-behavior during solution heat treatment, grain growth and also contribute to strengthening. However, this also means that the amount of silicon and magnesium, which is part of these phases, is not available for the following artificial aging and therefore does not contribute to precipitation hardening.

After solution heat treatment the material is quenched as fast as possible to room temperature. In most cases this is done by water quenching. The solubility of the solved elements decreases with decreasing temperature. When the quenching rate is high enough, the solute atoms stay dissolved in the matrix, resulting in a supersaturated solid solution (SSS). Due to the high temperature during the solution heat treatment, the vacancy concentration in the crystals of the material is higher than at room temperature. This can be explained by a higher movability of the atoms at elevated temperatures. Vacancies are normally annihilated at sinks like grain boundaries, jogs at dislocations or incoherent phases and particles, because their energy situation is unfavorable and the annihilation decreases the overall Gibbs energy of the system [11]. In case of rapid quenching the vacancies remain solved in the material, because there is not enough time for them to move to potential sinks. Therefore, an excess-amount of vacancies is quenched into the material, having a tremendous effect on the aging behavior in aluminium alloys. The higher amount of vacancies allow the solved atoms to diffuse, which would not be the case when only the equilibrium density of vacancies is present [12]. The exact way how vacancies are related to the precipitation of hardening particles will be discussed in the following section.

### **3.6 Aging of Al-6xxx series alloys**

To reach a maximum value of strength the alloy must be further heat treated artificially. Figure 10 shows a typical temperature profile during solution heat treatment, quenching and the following aging step. After solution heat treatment the material has so called T4 condition.

### 3.6.1 Influence of vacancies and natural aging

The thermodynamic situation of the supersaturated solid solution is not a stable one. Due to the high amount of excess vacancies the solute atoms begin to diffuse and build early clusters to reduce the energy of the system. This process is called natural aging, because it occurs without any artificial influence. This has a major impact on the following aging behavior of the alloy, as can be seen in [13] and [14]. In most cases the maximum reachable strength is decreased if the artificial aging is influenced by natural aging [15].

If there is a large enough time gap between quenching and the start of artificial aging, it leads to early stages of precipitation at low temperature. The distribution of these early precipitates (specially on different defects) promote inhomogeneous formation and growth of precipitates during aging treatments which leads to lower strength in compare to uniformly distributed precipitates that can be obtained with no natural aging. In the industry, in most cases it is not possible to carry out artificial heat treatment directly after quenching, giving the excess vacancies the possibility to annihilate at sinks. The decrease of excess vacancy density by annihilation leads to a coarser distribution and lower number density of early clusters in the material, resulting in a lower strength in peak-aging condition (T6).

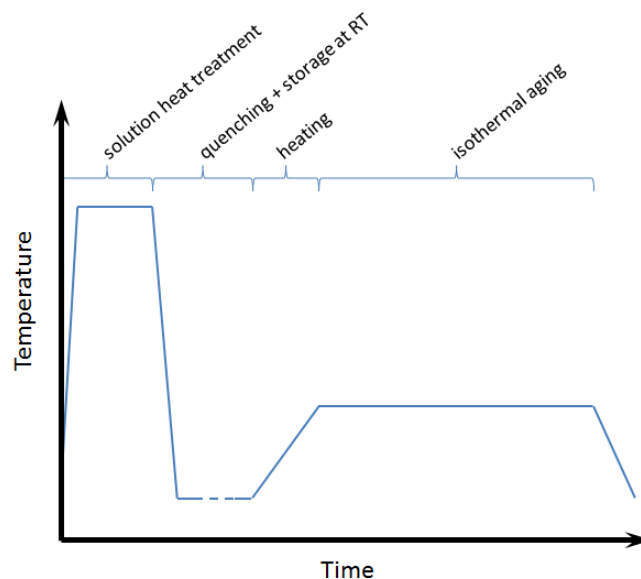


**Figure 10: Temperature profile during solution heat treatment, quenching and artificial aging of aluminium alloys.**

Therefore the storage at room temperature must be kept as short as possible. One possibility to overcome this problem is to use several elements to hinder the vacancies from annihilating at sinks to improve the artificial aging after natural aging [16]. Another approach is the use of special quenching techniques, as was shown recently by Pogatscher et.al [17].

### 3.6.2 The precipitation sequence in Al-Mg-Si alloys

If the artificial aging step is performed immediately after quenching, the precipitation sequence shown in Figure 11 is run through. A very good overview on the appearing precipitates is given by Povoden-Karadeniz et al. [18].

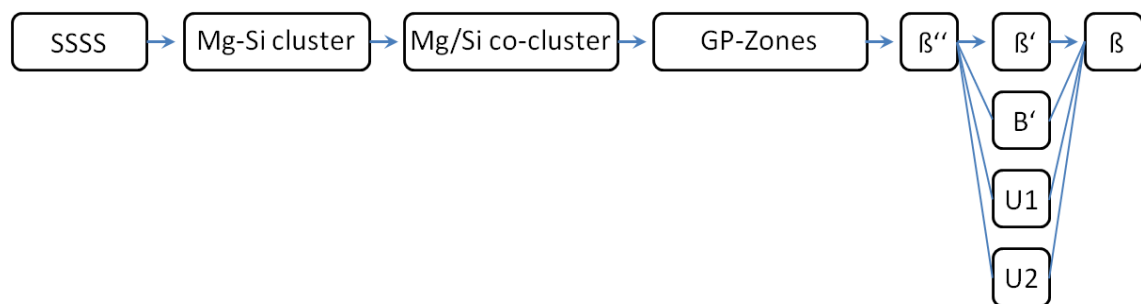


**Figure 11: Commonly accepted precipitation sequence in Al-Mg-Si alloys during aging.**

The supersaturated solid solution is the starting point, where the solute elements that are building the precipitates are completely solved in the matrix and the number density of vacancies is exceeding their equilibrium number. With increasing temperature during the heat treatment clustering occurs. In early literature the formation of pure Si and Mg clusters was suggested [19],[20]. What can be taken as assured is the formation of Mg/Si co-clusters. In this case the clusters consist of magnesium- und silicon atoms without a specific ordering of the atoms. The formation of these early stages of precipitation is discussed controversially in the literature and is believed to be highly dependent on the vacancy behavior. The only way to detect and investigate these early stages in terms of experimental work is atom probe tomography (APT). High resolution transmission electron microscopy (HRTEM) is also applicable, but the limits of resolution are rapidly achieved.

As the early clusters are further aged, monolayers of Mg and Si are built along crystallographic [100]-direction of the matrix. These layers are known under Guinier-Preston (GP)-zones. (GP)-zones appear in nearly every heat treatable

aluminium alloy. They were first described by Guinier and Preston in 1938 in Al-Cu alloys [21]. In Al-6xxx series GP-zones are assumed as metastable  $\text{Al}_2\text{MgSi}$  with a face-centered cubic (fcc) structure and are coherent with the Al-matrix. Due to their coherency they have a contribution to strength, which can be observed by hardness measurements during natural and artificial aging.

One of the most important precipitates in this sequence are so called metastable  $\beta''$  precipitates. The stoichiometry is believed to be  $\text{Mg}_5\text{Si}_6$ , which is affirmed by several studies that show a Mg/Si-ratio close to  $\sim 1$  [22],[23]. Small fluctuations can be described by a weak solubility of Al in this precipitate [24]. However, the exact composition highly depends on the chemical composition of the alloy.

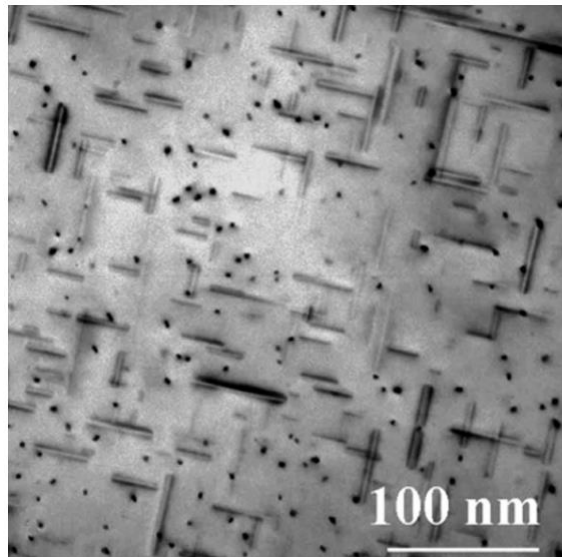


**Figure 12: Needle shaped  $\beta''$  precipitates in an Al-Mg-Si alloy, along  $\langle 001 \rangle$  zone axis [24].**

Figure 12 shows a TEM image of needle-shaped  $\beta''$  precipitates in an Al-Mg-Si alloy. The needles are orientated along the [100]-direction of the crystal and have elongation around 20 to 40nm and diameter of approximately 3-4nm. This is also in good accordance with other literature [22]. The small spherical precipitates are the cross section of the needles which are orientated along the  $\langle 001 \rangle$  zone axis of the material.  $\beta''$  precipitates are found to be the main precipitates contributing to strength and are therefore responsible for the peak strength of the material. The reason for this is the coherent to semi-coherent relation to the Al-matrix.

As aging continues, a couple of other metastable precipitates are formed, which can be co-existent with  $\beta''$ . The main phase is  $\beta'$  which has a composition of  $\text{Mg}_9\text{Si}_5$  or  $\text{Mg}_{1,8}\text{Si}$  with hexagonal structure.  $\beta'$  precipitates are rod shaped and significantly larger than  $\beta''$ , but also orientated along [100]-direction [25]. Three other phases, denoted as  $B'$ , U1 and U2 can also be present, depending on chemical composition of the alloy and thermal history. These phases are mainly differing in size, crystallographic structure and chemical composition. As they are not of high importance for this work, the interested reader is referred to Refs. [26],[27]. All mentioned phases have a semi-coherent relation to the Al-matrix.

The last step of the precipitation sequence is the formation of platelet-like stable  $\beta$  precipitates with a composition  $\text{Mg}_2\text{Si}$ . It has to be noted, that this phase is completely incoherent with the surrounding Al-matrix.

**Table 2: Chemical composition, crystallographic structure and morphology of precipitates occurring during aging of an Al-Mg-Si alloy [25]**

Phases observed during the precipitation hardening of Al-Mg-Si alloys			
Phase	Composition	Unit cell	Morphology <sup>a</sup>
GP (GP-I) [1]	$\text{Mg}_x\text{Al}_{5-x}\text{Si}_6$	Primarily monoclinic	Ranging from 1 to 3 nm spherical particles to needles of $\sim 2 \times 2 \times 20$ nm
$\beta''$ (GP-II) [2,3]	$\text{Mg}_5\text{Si}_6$	Monoclinic, $C2/m$ ; $a = 1.516$ nm, $b = 0.405$ nm, $c = 0.674$ nm; $\beta = 105.3^\circ$	Needles of $\sim 4 \times 4 \times 50$ nm
U1 (type A) [4,5]	$\text{MgAl}_2\text{Si}_2$	Trigonal, $P_{-3m1}$ ; $a = 0.405$ nm, $c = 0.674$ nm	Needles several hundred nanometres long, with $\sim 15$ nm diameter
U2 (type B) [4-6]	$\text{MgAlSi}$	Orthorhombic, $P_{nma}$ ; $a = 0.675$ nm, $b = 0.405$ nm, $c = 0.794$ nm	Needles several hundred nanometres long, with $\sim 15$ nm diameter
$\beta'$ [7]	$\text{Mg}_{1,8}\text{Si}$	Hexagonal, $P6_3/m$ ; $a = 0.715$ nm, $c = 1.215$ nm	Rods several hundred nanometres long, with $\sim 10$ nm diameter
$\beta'$ (type C) [5,9]	$\text{MgSi}_{-1}$	Hexagonal, $a = 1.03$ nm, $c = 0.405$ nm	Ribbons up to 1 $\mu\text{m}$ long
$\beta$	$\text{Mg}_2\text{Si}$	FCC (CaF type) $a = 0.639$ nm	Plates or cubes, up to 10–20 $\mu\text{m}$ across

<sup>a</sup> The dimensions given are only a rough indication; the actual values will depend strongly on the composition of the starting alloy and the heat treatment applied.

An overview about composition, structure and morphology of phases built during aging of Al-Mg-Si alloys is shown in Table 2. The  $\beta'$  (type C) precipitate is not subject of this thesis, but it shows that the exact precipitation sequence is not totally clear yet and is still subject to ongoing research.

### 3.6.3 Differential Scanning Calorimetry in Al-6xxx series alloys

A useful and easy to apply tool to investigate the precipitation sequence is differential scanning calorimetry (DSC). This technology can be used to visualize the energetic changes during a heat treatment of a material and allows the detection of phase transformations. Two types of measurement principles,



the power compensation DSC and the heat flux DSC are available. The scheme of the latter one is shown in Figure 13. In this case a sample (S) and a reference (R) material with equal weight are placed in a single measurement cell. Both materials are exposed to the same heating rate, which results in different temperatures of the sample and the reference caused by the difference in heat capacity.

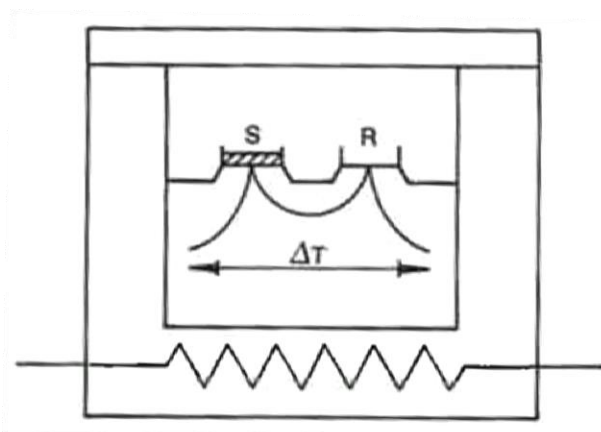


**Figure 13: Scheme of a heat flux-DSC showing position of a sample and a reference material within the measurement cell [28].**

The difference in temperature is converted into an energy equivalent, resulting in the DSC signal in Watt. Normally, this signal is also put into relation to the weight of the samples, which changes the measurement unit to W/g. In case of a power compensated DSC the sample as well as the reference are located in two separate cells where they are heated according to a given temperature profile. The different heat capacity of the sample and reference leads to a difference in needed heat flux. This difference is used to calculate the DSC signal, which is plotted over time or temperature, showing exothermic and endothermic reactions. Exothermic peaks are an effect of phase precipitation, but can also be related to solidification and recrystallization. The endothermic peaks are a result of phase dissolution or melting. Figure 14 shows a typical DSC plot of an AA6016 alloy directly after quenching. The measurement was performed with a heating rate of 10K/min and peaks corresponding to exothermic reactions are plotted in negative direction of the y-axis. Several exothermic and endothermic peaks are visible, marked with letters A to H. Peaks A and B are a result of precipitation and dissolution of early clusters and (GP)-zones, followed by peaks C and D which are related to the formation and dissolution of  $\beta''$  precipitates. According to the precipitation sequence  $\beta'$  and



stable  $\beta$  precipitates are built, which can be seen by peaks E to G. One should notice that it is not possible to distinguish between  $\beta'$ ,  $B'$ , U1 and U2 phases. It should be kept in mind that these plots show the reaction of the whole system. This means that reactions within the material could overlap and therefore result in a sort of superposition of peaks. This makes it difficult to distinguish between the reactions only via DSC investigations. When in doubt, additional investigation techniques, for example TEM or x-ray diffraction (XRD), are necessary. The large endothermic peak at the end of the DSC signal corresponds to the dissolution of all present precipitates.

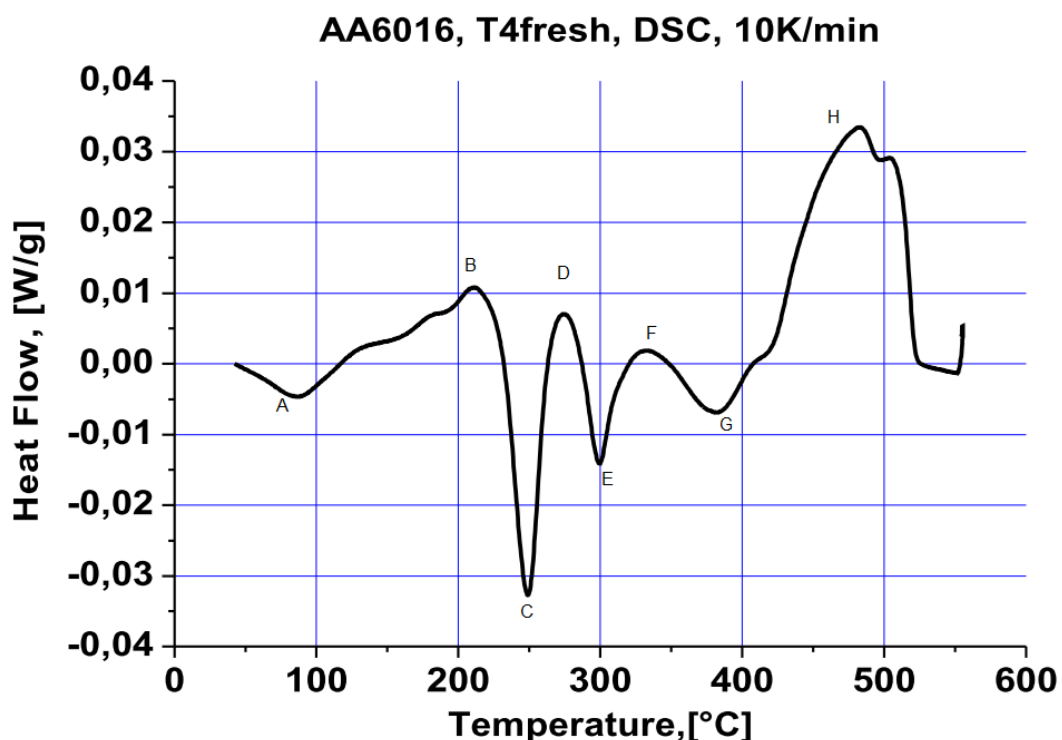


**Figure 14: DSC plot of a AA6016 alloy directly after solution heat treatment (T4) measured with a heating rate of 5K/min [29].**

This plot is highly accepted in literature and was investigated in several scientific papers [30],[31]. Especially publications of Gupta et al. give a brief investigation of DSC investigation in Al-Mg-Si alloys [32], [33]. They show the influence of heating rate, chemical composition and natural aging on the DSC plots.

### 3.6.4 Homogeneous and heterogeneous nucleation

To understand how particles can nucleate in a solid material, one has to investigate the energy that is needed to form precipitates. A good description of

the formation of precipitates is given in [34] and is the main background of this subsection. On one hand energy is needed to build the new surface of precipitating particles, given by  $\Delta G_{\text{surf}}$ . This is basically the interfacial energy  $\gamma$  between precipitates and matrix. Values of the interfacial energy cannot be determined directly, only by measurement of values that depend on this energy. A very good way to calculate the interfacial energy is the Generalized Broken-Bond (GBB) model of Sonderegger and Kozeschnik [35].

The other energy that is needed to form precipitates is the specific volume free energy change  $\Delta G_{\text{vol}}$ , which is the energy required to transform one unit volume of the matrix into one unit volume of the precipitate.  $\Delta G_{\text{vol}}$  can be split in two parts, one contributing to the chemical events in the material and a mechanical part, which is shown in following equations 1 and 2:

$$\Delta G_{\text{vol}} = \Delta G_{\text{vol}}^{\text{chem}} + \Delta G_{\text{vol}}^{\text{el}}. \quad (1)$$

$$\Delta G_{\text{vol}} = -\frac{d_{\text{chem}}^{\beta}}{v^{\alpha}} + \Delta G_{\text{vol}}^{\text{el}}. \quad (2)$$

Equation 2 shows that the chemical part depends on the chemical driving force  $d_{\text{chem}}^{\beta}$  to form the precipitate and  $v^{\alpha}$  being the molar volume of the matrix. The mechanical part  $\Delta G_{\text{vol}}^{\text{el}}$  will be discussed at the end of this subsection. Equation 3 is used to obtain the free energy of nucleus formation  $\Delta G_{\text{nucl}}$ , where  $\rho$  is the radius of the precipitate.

$$\Delta G_{\text{nucl}} = \frac{4}{3}\pi\rho^3 \cdot \Delta G_{\text{vol}} + 4\pi\rho^2 \cdot \Delta G_{\text{surf}} \quad (3)$$

As can be seen, the specific volume energy change is multiplied with the volume of the precipitate and the interfacial energy is multiplied with the surface area of the particle. If  $\Delta G_{\text{nucl}}$  is plotted over the radius some very basic statements about the stability of nuclei can be made. This plot is shown in Figure 15. The interfacial energy always has a positive contribution to the free energy of nucleus formation, which has a destabilizing effect on the nuclei. On the other hand,  $\Delta G_{\text{vol}}$  always has a stabilizing contribution, because it decreases the overall energy and the system always tries to reach a state with minimum energy. The extremum of  $\Delta G_{\text{nucl}}$ , which is here marked as  $G^*$ , is of high

importance. This energy value is located at a specific radius  $r^*$ . If the nuclei have a size below this radius it is energetically not possible for them to grow and it will dissolve again. If the nuclei are larger than that critical radius  $r^*$  they become stable and their growth is energetically favorable. Therefore  $G^*$  is called the critical nucleation energy that a system must overcome to make precipitation and growth possible.

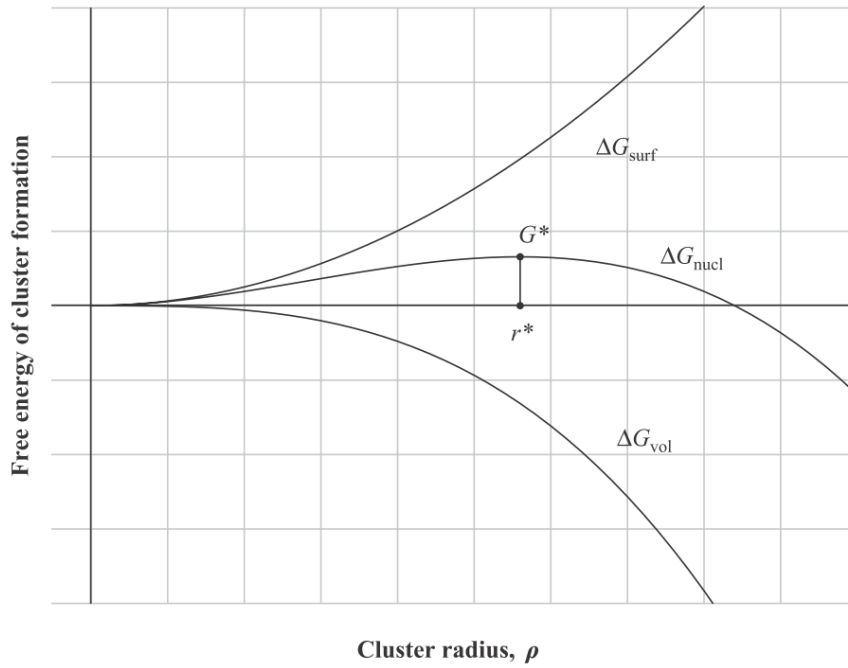


**Figure 15: Free energy of cluster formation plotted over precipitate radius, explaining the critical nucleation radius and the energy barrier for precipitation [34].**

Equations 4 and 5 show the dependence of  $r^*$  and  $G^*$  on the interfacial energy  $\gamma$ , chemical driving force  $d_{\text{chem}}^{\beta}$ , the molar volume  $v^{\alpha}$  and  $\Delta G_{\text{vol}}^{\text{el}}$ .

$$r^* = -\frac{2\Delta G_{\text{surf}}}{\Delta G_{\text{vol}}} = \frac{2\gamma}{\frac{d_{\text{chem}}^{\beta}}{v^{\alpha}} - \Delta G_{\text{vol}}^{\text{el}}} \quad (4)$$

$$G^* = \frac{16\pi}{3} \frac{(\Delta G_{\text{surf}})^3}{(\Delta G_{\text{vol}})^2} = \frac{16\pi}{3} \frac{\gamma^3}{\left(-\frac{d_{\text{chem}}^{\beta}}{v^{\alpha}} + \Delta G_{\text{vol}}^{\text{el}}\right)^2} \quad (5)$$

As coherent precipitates grow, they disturb the surrounding lattice because of volume misfit. This leads to stress in the matrix lattice which gives an additional barrier for nucleation, because the energy contribution of this effect is always positive. This energy is the mechanical part of  $\Delta G_{\text{vol}}$  and is given in equation 6.

$$\Delta G_{\text{vol}}^{\text{el}} = \frac{E^{\alpha}}{1 - \nu_p^{\alpha}} (\varepsilon^*)^2 \quad (6)$$

The energy of the elastic misfit  $\Delta G_{\text{vol}}^{\text{el}}$  depends on the elastic modulus of the matrix  $E^{\alpha}$ , the poisons ratio of the matrix  $\nu_p^{\alpha}$  and the linear elastic misfit  $\varepsilon^*$ , which can be calculated out of the volumetric misfit  $v^*$ , with  $\varepsilon^* = v^*/3$ .  $v^*$  depends on the difference in molar volume of the matrix  $v^{\alpha}$  and the molar volume of precipitate phase  $v^{\beta}$ , which is shown in Equation 7.

$$v^* = \frac{v^{\beta} - v^{\alpha}}{v^{\alpha}} \quad (7)$$

In some cases, the elastic misfit stress and as a consequence its energy contribution become so high, that nucleation is completely suppressed in a perfect crystal lattice. In reality the lattice of a crystal is not perfect and contains several defects. These defects also can deform the lattice, leading to a stress field. It can become possible for precipitates to nucleate at these points, because the stress fields of the defects and the nuclei annihilate each other, leading to an energetic situation where nucleation is possible. This effect is called heterogeneous nucleation. Typical nucleation sites for this type of nucleation are vacancies, solute elements, edge dislocations, grain boundaries or incoherent inclusions.

### **3.6.5 Impact of precipitates on strength – precipitation hardening**

As mentioned in previous sections, the precipitates have a large impact on the strength of the alloy. The increase of strength is achieved by precipitation hardening. The precipitates act as a barrier for dislocation movement. A key parameter for this effect is the coherency of the precipitates with the matrix, which is described in Figure 16.

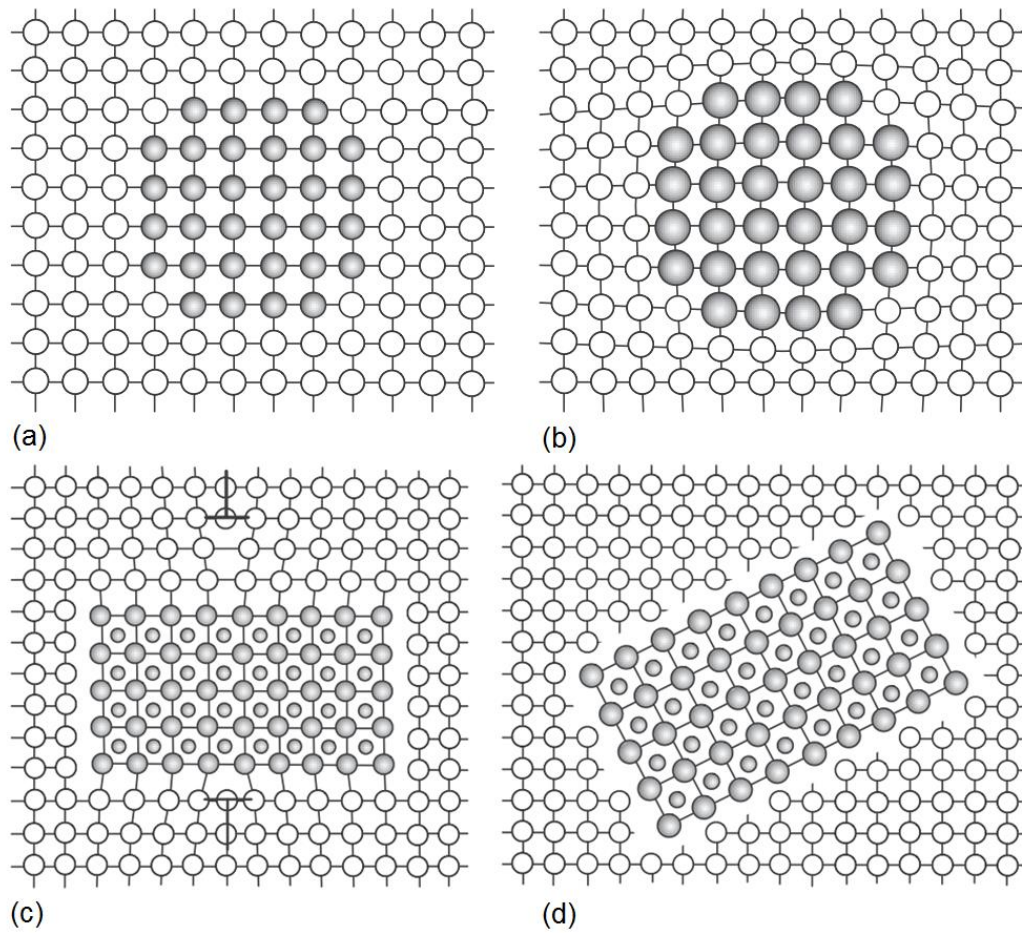


**Figure 16: Coherency of precipitates with the surrounding matrix; complete coherency without (a) and with volumetric misfit (b); semi-coherent (c) and incoherent (d) precipitates [34].**

In case of small coherent particles the shear-mechanism is active. This means that the precipitates are just sheared with a value  $b$ , where  $b$  is the Burger's vector of the dislocation. This effect can be seen in Figure 17.

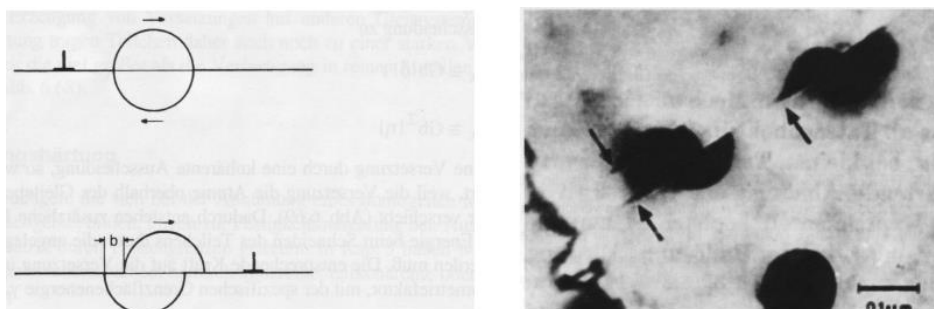


**Figure 17: Shear mechanism on a precipitate during dislocation movement [36].**

The formation of the new surface needs energy which is a barrier for the dislocation movement. As the number of precipitates and particle size rises, the energy needed to produce a new surface is increased until a point where the shearing of the particles is not energetically favorable. The dislocations start to

pass the precipitates, leaving a typical dislocation ring around the precipitate, which is called Frank loop. This mechanism is called Orowan mechanism and is shown in Figure 18.

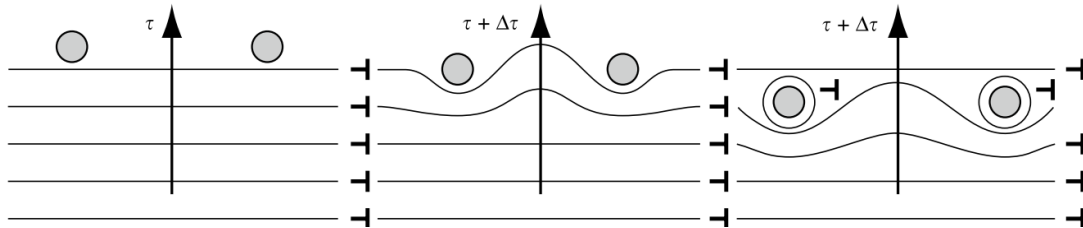


**Figure 18: Orowan mechanism; Dislocations pile up at precipitates and then pass by, leaving a dislocation loop around the precipitate [37].**

The contribution to strength increases with decreasing particle distance. In case of aluminium alloys, the minimum particle distance in combination with a favorable coherency situation is reached by  $\beta''$  precipitates, giving the alloy its peak strength. As aging goes on, in general the particles grow at the expense of smaller particles (Ostwald ripening), leading to an increase in particle size and a decrease in number density. This results in a higher distance between the particles, causing lower strength of the material and the material goes in over-aged condition. In Al-Mg-Si the precipitates following  $\beta''$  are typical for this situation. Their size is bigger than the one of the  $\beta''$  precipitates and also their decreasing coherency with the matrix has a negative effect on strength. Experimentally this can be shown easily via hardness measurements during the artificial aging process, which is shown in Figure 19. The hardness increases until approximately 225°C is reached and decreases as temperature rises. Compared to the DSC plot in Figure 14, one can see that the hardness increases at the same temperature at which the exothermic peak of  $\beta''$  formation is located. The decrease in hardness can be explained by the formation of the precipitates following the  $\beta''$  ( $\beta'$  and ongoing), which can also be seen when compared with the DSC plot.

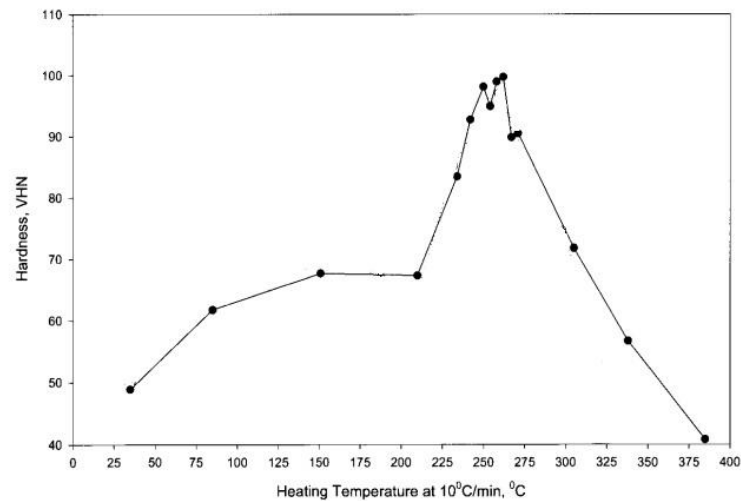


**Figure 19: Hardness values during non-isothermal heat treatment with a heating rate of 10K/s in an Al-0.4%Mg-1.3%Si-0.25%Fe alloy [33].**

In industrial processes, the artificial aging is performed during an isothermal heat treatment. In this case the individual precipitates form at certain temperatures and duration. This circumstance can also be illustrated via hardness measurements during an isothermal heat treatment, performed for different durations.

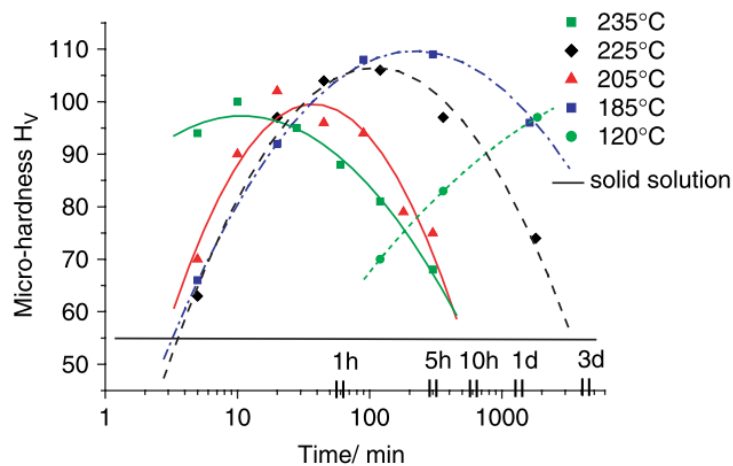


**Figure 20: Hardness as a function of annealing time at various isothermal temperatures in AA6016 [22].**

Figure 20 shows the result of such a test. The maximum hardness is reached with a temperature of 185°C after approximately 5h soaking time. At higher temperatures the precipitation starts earlier, but the peak hardness of the alloy cannot be achieved. At lower temperatures an increase of hardness is observed after a quiet long annealing time and also the maximum hardness is lower than the hardness of the peak-aged condition.



## 4 Experimental

In this thesis, two alloys are investigated. One is an industrial AA6016 alloy, which contains several accompanying elements. To show the effect of absence of these elements on the microstructure, a laboratory made pure alloy which is representing a ternary system was investigated. First of all the grain size was determined by metallography and light microscopy. The kinetics during precipitation was examined via DSC-measurements. To understand how the absence of accompany elements affect the industrial way of artificial aging, hardness measurements and TEM-investigations were performed during aging heat treatment likewise to an industrial procedure.

### 4.1 Used material

The chemical composition of the investigated materials is shown in Table 3.

**Table 3: Chemical composition of used materials in wt%.**

type	Mg	Si	Fe	Ti	Cu	Mn	Zn	Al
AA6016	0.35	1.10	0.16	0.02	0.08	0.07	0.01	bal.
Lab-made	0.38	1.08	0.02	-	-	-	-	bal.

The amount of magnesium and silicon is nearly similar. The very small iron content in the laboratory-made alloy can be explained by the purity of the aluminium which was used to produce this material. Compared to the industrial alloy this value is negligible. Special attention must be paid to the amount of titanium in the industrial material, which seems to be low, but is sufficient to induce a grain refinement during casting. Small amounts of copper, manganese and zinc are present. All these elements are absent in the laboratory-made pure alloy, which should lead to differences in microstructure and precipitation kinetics compared to the industrial AA6016. Intermetallic phases built by accompanying elements contain some Si and Mg, which leads to a slight decrease of these elements available for the formation of precipitates during artificial aging of industrial alloy. Considering this effect, both alloys have almost the same amount of Si and Mg.



The laboratory-made alloy was produced via Opticast-technology which leads to a pretty similar as-cast structure as in the industrial process. The Opticast samples were then homogenized for approximately 12h at 540°C, followed by hot rolling to a thickness of 1.5mm. The Opticast sample and the rolled material are shown in Figure 21.



**Figure 21: Opticast sample (a) and the used laboratory-made pure alloy after rolling (b).**

The material was then solution heat treated for 0.5 hours at 540°C to achieve T4 condition. This procedure is pretty similar to the industrial process. The industrial AA6016 alloy was delivered as sheet with 1.5mm thickness, in T4 condition.

## 4.2 Metallography

Metallographic samples were produced, to examine the differences in grain size of both alloys in T4 condition. Therefore 10x10mm large pieces were cut out of the sheets with a water-cooled cut-off machine Struers “Discotom 2”. Samples were then embedded in an electrically conducting embedding compound. This was performed in a hot mounting press Struers “PredoPress” at a maximum temperature of approximately 120°C. The orientation of the samples within the embedding was chosen in a way to make the investigation of a plain perpendicular to the rolling direction possible. In the next step the samples were grinded with abrasive paper of different grit size, following the sequence, 500-1200-2400-4000. This was followed by polishing in steps 9μm-3μm and OPS (Oxide Polishing Suspension).

The samples were etched electrolytically in a Barker’s etchant, which consists of 600ml distilled water and 15ml of tetrafluoboric acid. The impressed voltage had a value of 25V and the etching was performed in 4 steps with a residence time of approximately 30s respectively. After the second etching step the

---

samples were again polished ( $3\mu\text{m}$ ) for a few seconds to provide a more reactive surface. The samples were then investigated with a light microscope under use of differential interference contrast (DIC).

### **4.3 DSC measurements**

Samples with a diameter of 6mm and a thickness of 1.5 mm were stamped out of both alloys and grinded to a weight of 70mg. The reference material was high purity 99.9%-aluminium, with the same geometry and weight. To provide a freshly solution-annealed material and to suppress the effect of natural aging, the already in T4 condition delivered industrial alloy was again solution heat treated for 0.5h at  $540^{\circ}\text{C}$ . Annealing was performed in a Bähr-dilatometer DIL 805 to obtain a highly accurate temperature profile. The quenching was done by high purity helium, providing a quenching rate of 100K/s, which is assumed to be slower than the quenching rate achieved under the use of water quenching. The slower quenching has an effect on the vacancy concentration, but the high reproducibility of the quenching rate makes the comparison between the laboratory-made and the industrial material more accurate. Directly after quenching the samples were placed into the measurement cell of the DSC together with the reference material. This step was performed as fast as possible to minimize the time for vacancies to be annihilated at sinks. Time between quenching and start of the DSC run was about 60s.

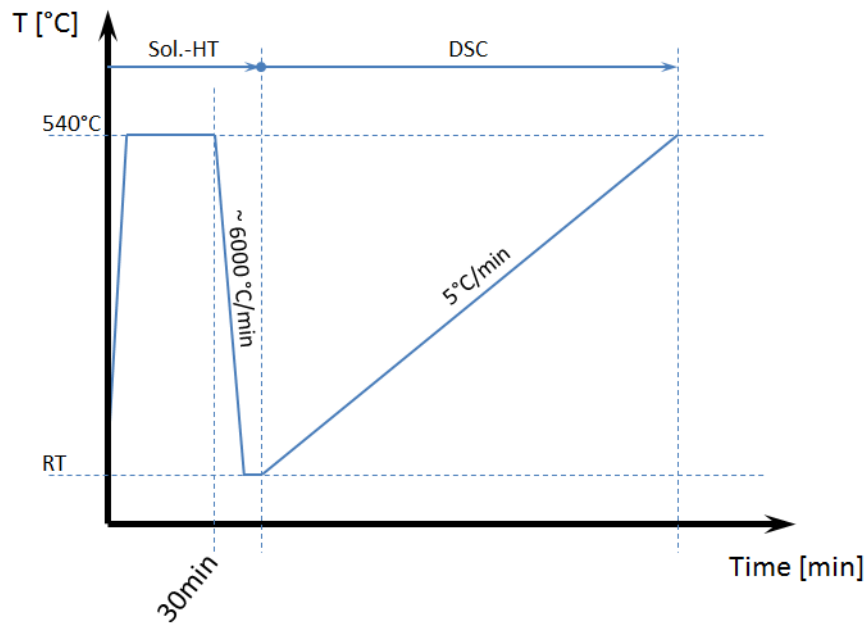


**Figure 22: Heat treatment sequence for DSC measurements.**

The DSC runs were performed under nitrogen flow (5l/h) with a heating rate of 5K/min from 30°C to 540°C. In case of the laboratory-made pure alloy the measurements were repeated three times, giving highly reproducible results. The detailed temperature profile during these experiments is shown in Figure 22. Also a baseline with two pure aluminium samples with a heating rate of 5K/min was recorded.

## 4.4 Hardness measurements

Brinell hardness measurements according to DIN EN ISO 6506 were performed at different steps during an industrial aging heat treatment. The used indenter diameter was 1mm and a force of 10kp was applied for 10s. Small plates with dimensions 10x10mm were cut out of the plates and grinded by hand on both sides with abrasive paper in a sequence 500-1200-2400-4000 grit size, to provide a good surface for the test. Of course this was done for both types of material.

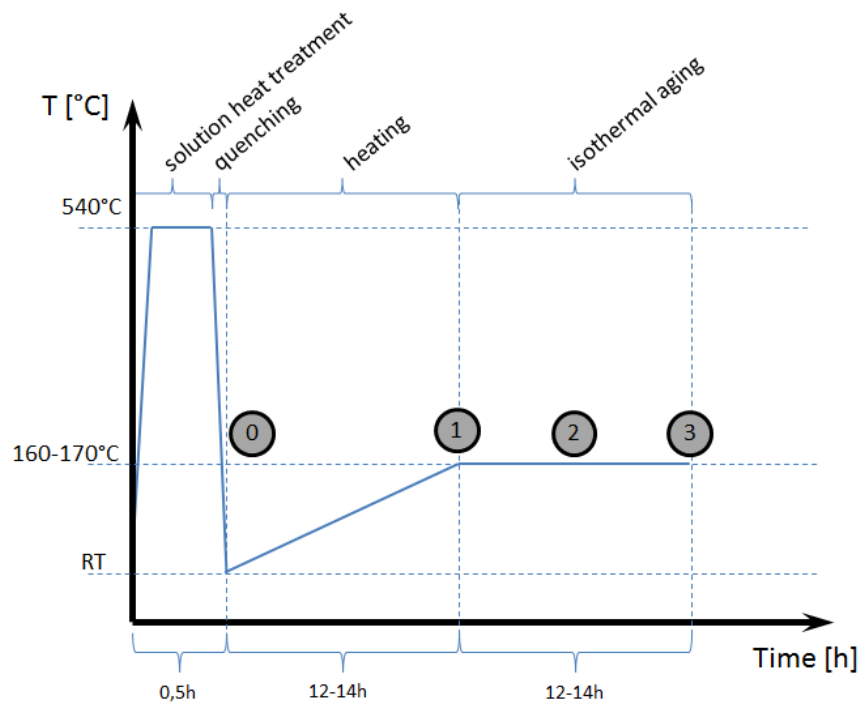


**Figure 23: Industrial heat treatment process; numbers 1-4 show specific points where investigations were performed.**

Figure 23 shows the applied industrial heat treatment process. Temperature and annealing time are given in rough ranges due to confidentiality. The exact values are of course known by the author. The heat treatment was performed in a Bähr-dilatometer DIL 805 to reach a maximum accuracy. The quenching step was executed with high purity helium. To show the hardness evolution during this industrial heat treatment, the process was performed several times until different conditions (marked with 0 to 4) were reached, which are also shown in Figure 23. The process was interrupted at these points by quenching with high purity helium (100K/s) to freeze the microstructure. For each condition, the process was started with a fresh sample from the very beginning, which results in 4 runs for each type of alloy. The measurements were done using an Emco M1C 010 micro- and low load hardness testing machine. For each sample, at least four hardness measurements were executed, depending on the scatter of results.

Condition 0, which is basically the as-quenched situation, needs a special treatment because of its high tendency to natural aging. To suppress the formation of clusters in the material after quenching, the samples were stored in liquid nitrogen during transport to the hardness testing machine and

---

measurements were done after the samples were reheated to room temperature.

## **4.5 TEM investigations**

Samples in condition 1 to 3, which were used for hardness tests, were also used for TEM investigations to determine precipitate size and number density. TEM studies are unnecessary in condition 0, since the early clustering is hard investigable via TEM and is also not a key issue of this work.

The 1.5mm thick samples were grinded both sides to a thickness of 10 $\mu$ m. In the last step an abrasive paper with a grit of 4000 was used. To reach the final thickness that is needed for TEM investigations, the samples were electropolished in a Struers "TenuPol-5", using an electrolyte consisting of 30% nitric acid in methanol solution at -24°C.

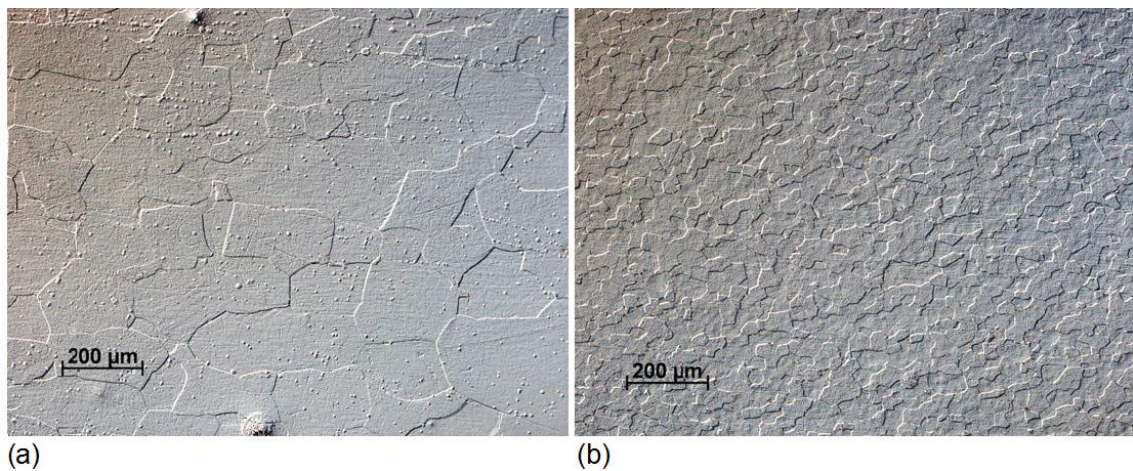
The TEM investigations were executed in a FEI Tecnai F20 transmission electron microscope, equipped with a field-emission gun, an energy-dispersive x-ray (EDX) device and a high-angle annular dark field (HAADF) and scanning transmission electron microscope (STEM) detector. The operation voltage is 60-200kV.

## 5 Results

This chapter sums up relevant results from all experiments described in chapter 4 and a close discussion will be given in chapter 6.

### 5.1 Metallography

The investigations were performed at laboratory-made pure and industrial AA6016, both in T4 condition.



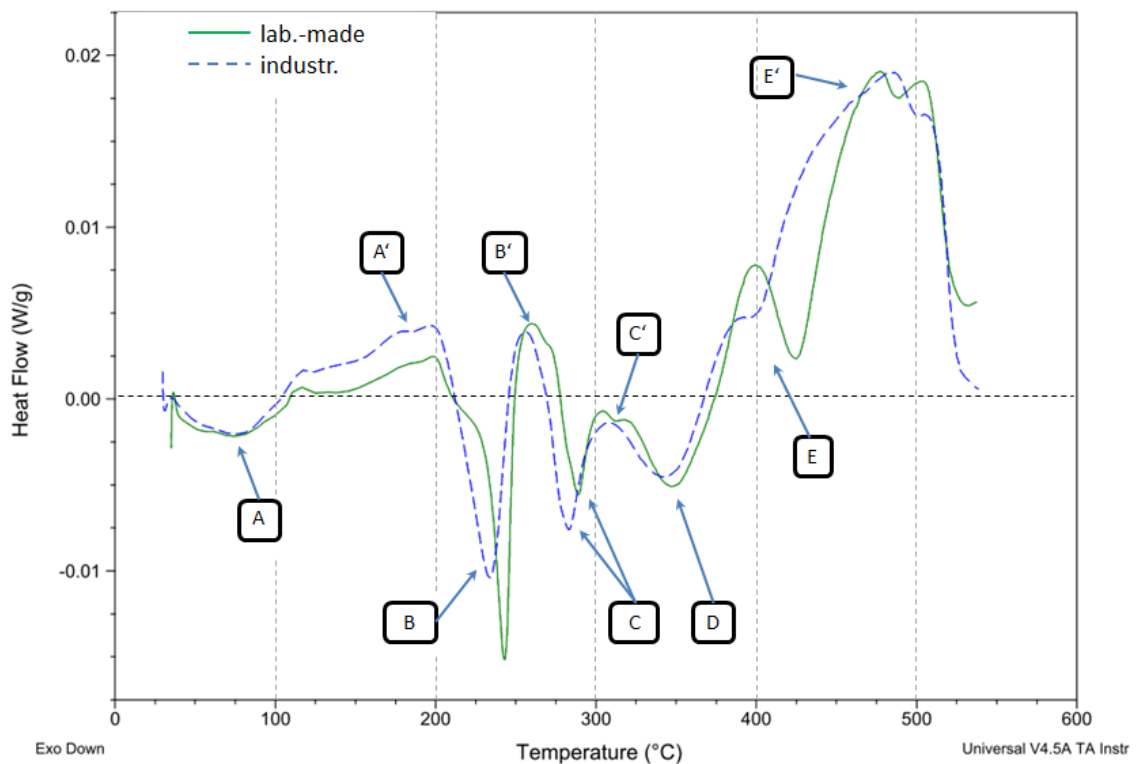
**Figure 24: Micrographs (100x) of laboratory-made alloy (a) and industrial AA6016 (b) in T4 condition, showing the effect of grain refining elements.**

Figure 24 shows the resulting micrographs. In Figure 24(a) the micrograph of the laboratory-made pure alloy is shown. The picture shows very large grains in the center of the material with a grain size of approximately 250 μm. Grains are elongated in horizontal direction due to hot rolling. Compared to this, the micrograph of the industrial AA6016 shows a significant smaller grain size of approximately 50 μm and also a slight elongation in horizontal direction caused by rolling, which can be seen in Figure 24(b).

### 5.2 DSC measurements

Figure 25 shows the results of the DSC measurements for the laboratory-made pure, as well as the industrial AA6016 alloy after the subtraction of the baseline. The heat flow is plotted in W/g over a temperature range between 0°C and 600°C. Exothermic reactions are characterized by a negative heat flow.

In case of both alloys some exothermic (A-E) and endothermic peaks (A'-E') on DSC curves are visible. The exothermic peaks contribute to precipitation and the endothermic peaks to the dissolution of the precipitates. The exothermic peaks in the industrial alloy are located at 80°C, 230°C, 285°C and 350°C respectively. One should also notice a saddle point at around 400°C in the industrial alloy. The exothermic peaks are always followed by endothermic peaks which are located at 190°C, 260°C, 310°C and around 490°C.



**Figure 25: DSC plot of industrial (dashed) and laboratory-made pure (solid) material directly after solution heat treatment, measurement performed with 5K/min.**

The laboratory-made pure alloy follows a pretty similar characteristic. The extreme values of exothermic reactions are located at 80°C, 245°C, 295°C and 360°C. Compared to the industrial material one additional exothermic reaction is located around 425°C. The endothermic peaks which contribute to dissolution appear at 190°C, 270°C, 310°C and also at 490°C. Subsumed, some exothermic reactions of the laboratory-made alloy occur at higher temperatures than the exothermic reactions of the industrial AA6016 alloy.

### 5.3 Hardness measurements

The results of the hardness measurement are shown in Figure 26. The plot also shows the temperature profile of the industrial heat treatment to make the allocation of the hardness values to the condition of the alloy easier. The exact measured values are shown in Table 4.

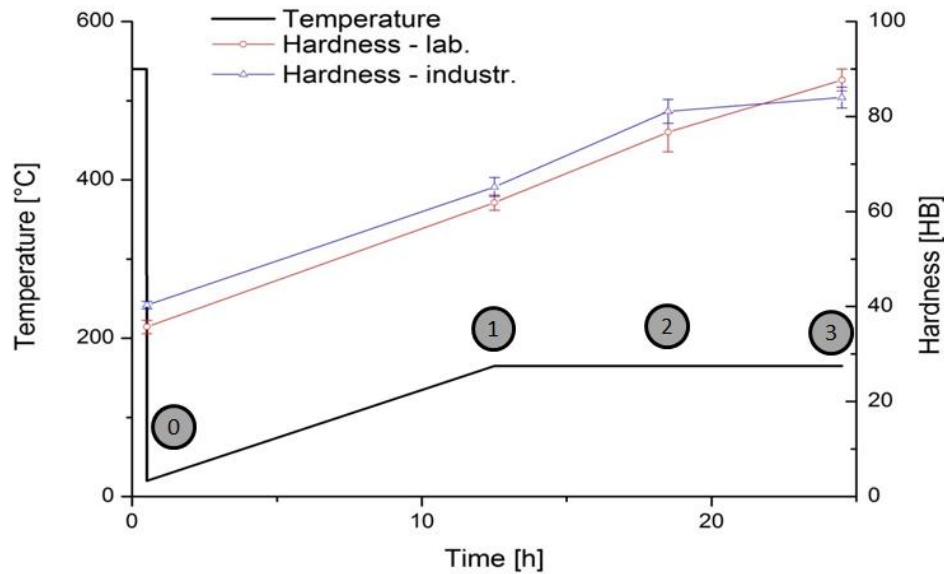


**Figure 26: Hardness as function of annealing time through the industrial heat treatment for laboratory-made and industrial material.**

In the as-quenched state, the alloys show low hardness of 35.7HB in the laboratory-made pure alloy and 40.3HB in the industrial material. As aging goes on, the hardness is increased to values of 61.9HB and 65.2HB, respectively. In the middle of the isothermal section this trend continues, leading to values of 76.8HB (lab.-made) and 81.1HB (industry). The industrial alloy then shows stagnation in increase of hardness during the last section of the heat treatment, leading to a final value of 84HB. Compared to this, the laboratory-made pure alloy shows a further significant increase in hardness, with a result of 87.7HB. One should keep in mind the spreading of these values, which are listed in Table 4 in combination with the final values and are illustrated as error bars in Figure 26.

**Table 4: Results of Brinell hardness tests at different conditions of the alloys during the industrial heat treatment.**

sample-ID	hardn. in cond. 0	hardn. in cond. 1	hardn. in cond. 2	hardn. in cond. 3
lab.-pure	35.7±1.4	61.9±2	76.8±2.5	87.7±2.2
industr. AA6016	40.3±0.8	65.2±1.6	81.1±4.1	84±2.3



## 5.4 TEM investigations

This subsection shows the results of performed TEM investigations at different conditions during the industrial heat treatment, which is used for aging. Condition 1 shows the material at the end of the heating ramp. Condition 2 contributes to the middle of the isothermal step and condition 3 shows the materials at the end of the industrial heat treatment. All three conditions are also shown in Figure 23.

### 5.4.1 TEM - condition 1

Both alloys in condition 1 were investigated via TEM-bright field and dark field imaging. Also EDX was used to show the chemical composition of the existing phases.

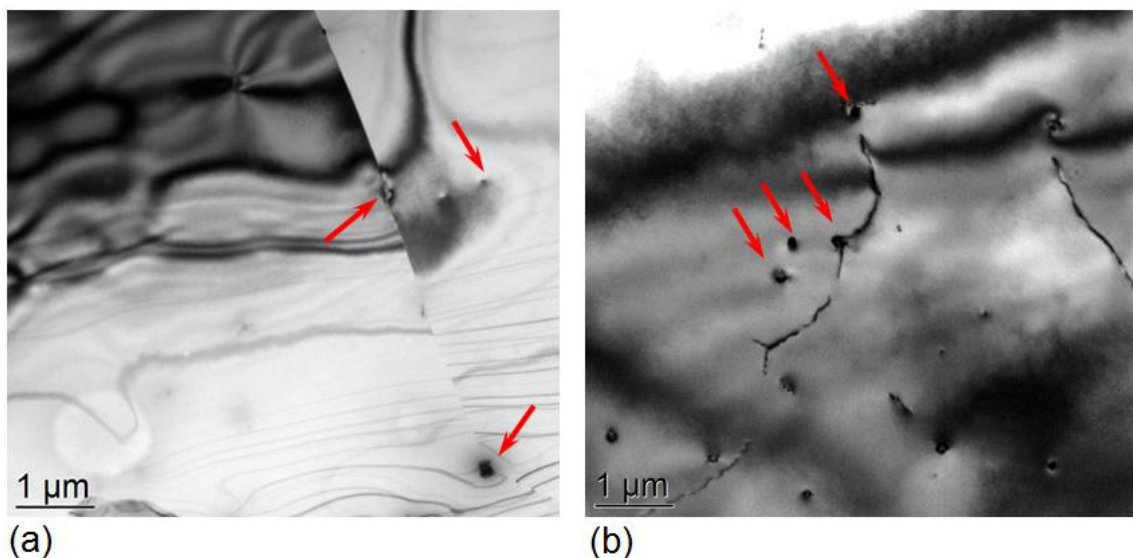
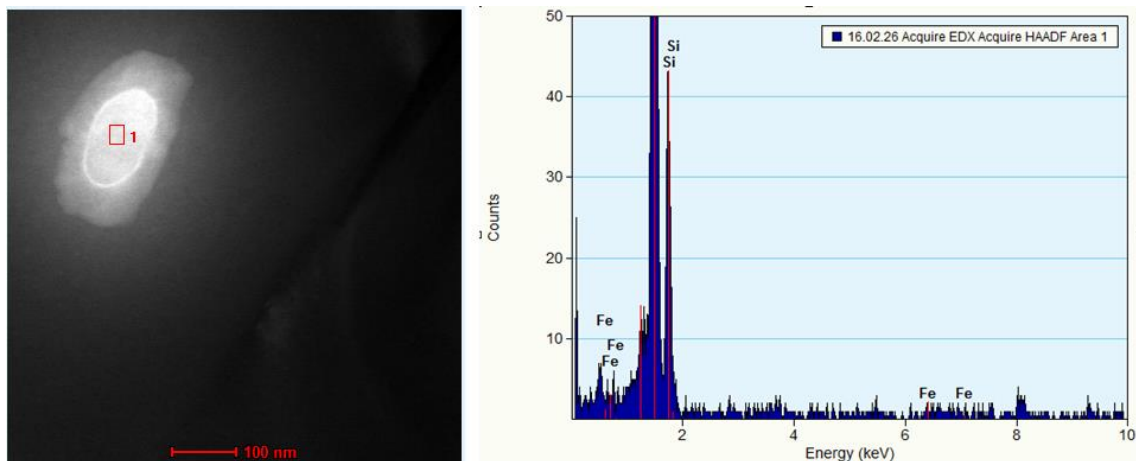


**Figure 27: TEM bright field images of condition 1 after a 12h in industrial heat treatment; Small dispersoids at grain boundaries and in bulk material of lab.-made alloy (a); larger precipitates in bulk with pinned dislocations in AA6016 (b).**

Figure 27(a) shows a bright field image of the laboratory-made pure Al-Mg-Si alloy. Three grain boundaries are visible, which meet at the right bottom of the image. In this triple-point a dispersoid is located. More small dispersoids with a diameter of approximately 100-150nm are positioned at the grain boundary and also within the grains. All dispersoids were marked with red arrows. The gray and black lines in the picture are caused by different thickness and deformation of the sample.

A TEM image of the industrial AA6016 at the same magnification is shown in Figure 27(b). A number of dispersoids is visible, some of them marked with arrows, having a size around 100nm to 200nm. The dark lines contrasted between some dispersoids contribute to dislocations.

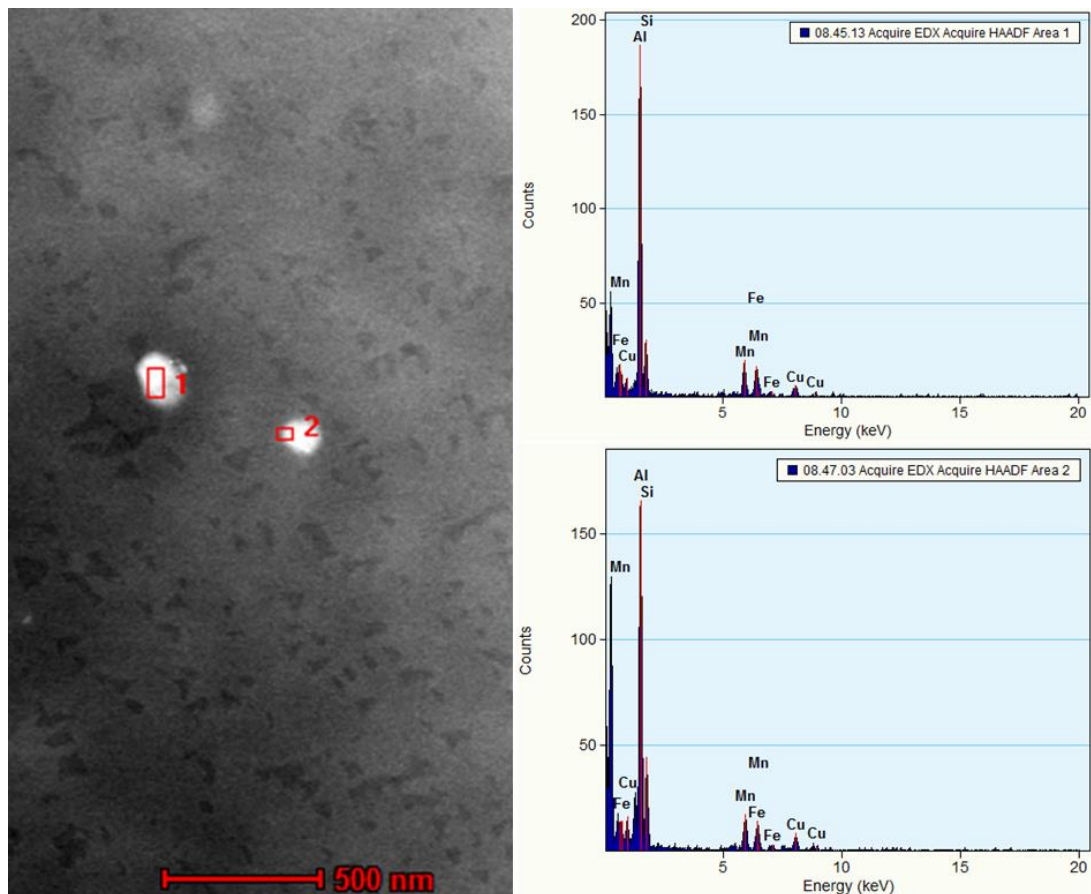
To examine the chemical composition, EDX-tests were performed. The results for particles detected in the laboratory-made pure alloy are shown in Figure 28.



**Figure 28: Dark-field image and EDAX analysis of AlFeSi-dispersoids in lab.-made alloy.**

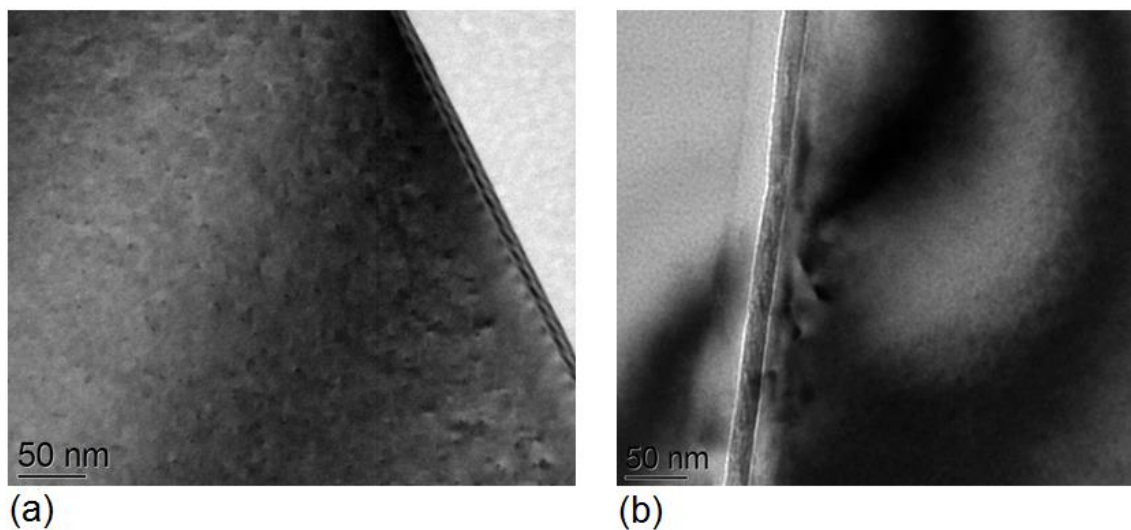
The investigated particle had a size of about 100nm. The left picture was taken from the dark field detector of the TEM at a magnification of 160kx. The red marked area (1) in the middle of the particle was investigated via EDX in STEM mode and the results of the EDX analysis is the spectrum shown in the left picture of Figure 28. The large peak contributes to aluminium. Also a quiet large amount of silicon was detected in the particle, accompanied with small amounts of iron. This means the particles are AlFeSi dispersoids, which were formed during casting and homogenization.

Figure 29 shows the investigation of the particles which were observed in the industrial AA6016 material. The left picture again shows a dark field image. Two dispersoids with a size of approximately 150nm are visible. Again, the areas which are marked with red boxes were investigated via EDX in STEM mode. Both areas showed a similar composition, as can be seen in the spectra shown at the right top and right bottom of Figure 29. Main elements are aluminium, silicon, iron and manganese. Also a small amount of copper was detected.



**Figure 29: Dark field TEM-image and EDAX analysis of AlFeMnSi-dispersoids also containing small amounts of copper in AA6016.**

At higher magnifications no significant precipitation is visible. One may suspect signs of precipitates in Figure 30(a), which shows the laboratory-made pure alloy. But this could not be confirmed at even higher magnifications or via selected area diffraction.

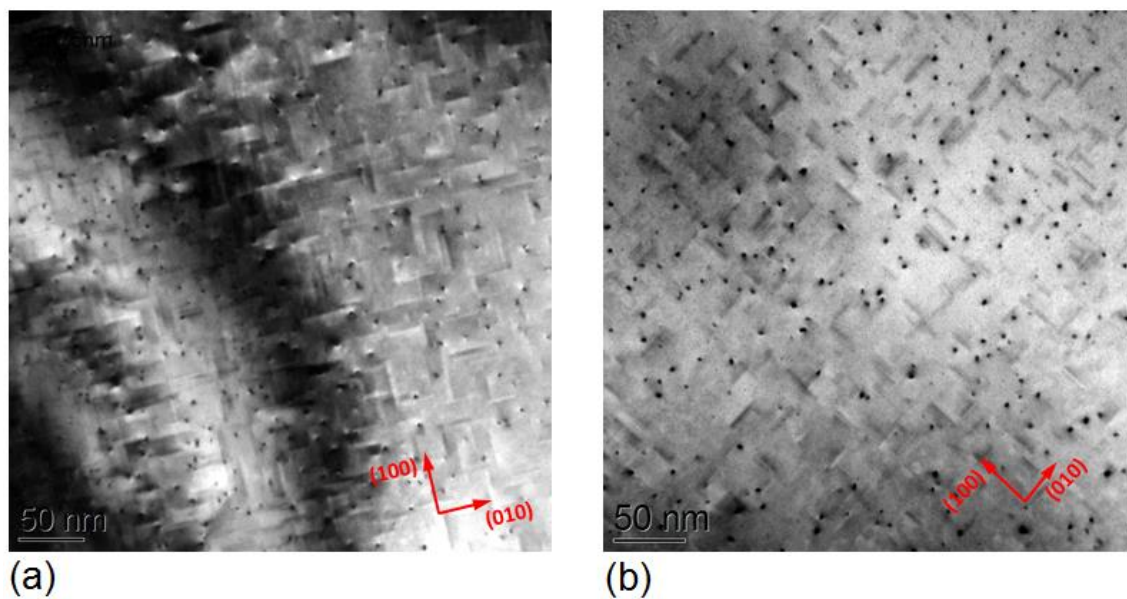


**Figure 30: Brightfield TEM-image of lab.-made (a) and ind. material (b) at condition 1 at the end of the heating ramp in industrial heat treatment, showing no precipitation.**

Figure 30(b) shows the TEM-image of the industrial AA6016 alloy, where also no precipitates are visible. The areas with different contrast belong to two neighboring grains. The difference in contrast is a result of different crystal-orientation in the grain and the line between these areas is the grain boundary.

#### 5.4.2 TEM – condition 2

Condition 2 is present at the middle of the isothermal section of the industrial heat treatment process. The TEM-investigations in this condition were performed via bright-field imaging and selected area diffraction.



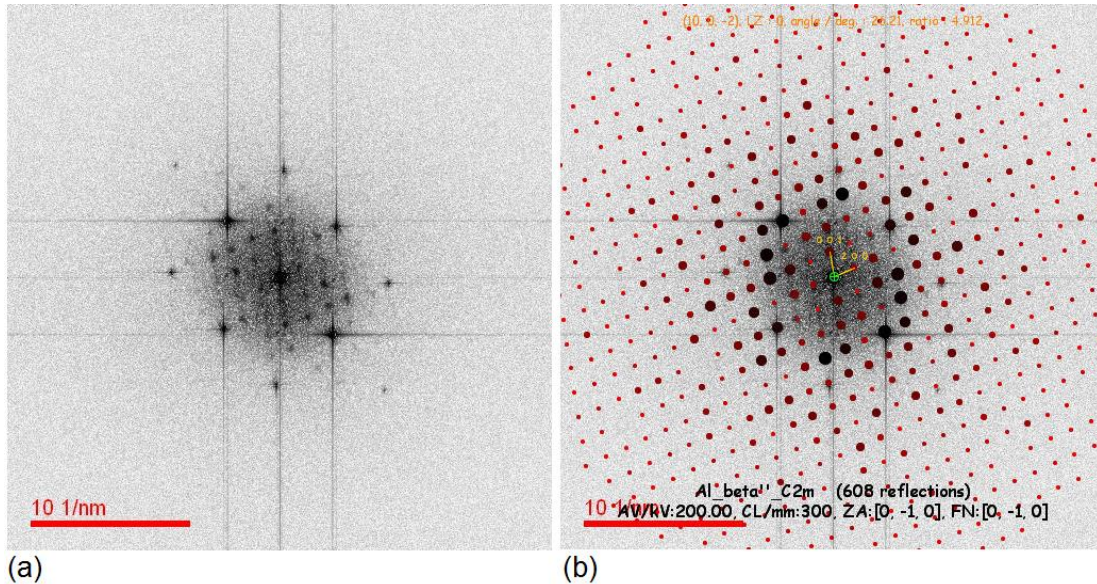
**Figure 31: Brightfield TEM-image of lab.-made (a) and ind. material (b) at condition 2 after 18h in industrial heat treatment showing  $\beta''$  precipitates orientated along  $\{001\}$  directions.**

Figure 31 shows the transmission electron microscope images of the laboratory-made pure (a) and the industrial AA6016. The samples were therefore tilted in  $[001]$  direction of the matrix crystal.

In both materials small precipitates are visible. They are needle-shaped and have elongation of approximately 20nm and a diameter of 4nm. All precipitates are orientated in  $\{001\}$  directions of the aluminium matrix. Therefore, the spherical particles appearing in both images are just the cross-section of the needles that are orientated in  $[001]$  direction. All these parameters indicate the presence of  $\beta''$  precipitates.



To prove this, selected area diffraction (SAD) patterns of the precipitates orientated along [001] were recorded, because they give the highest contrast during imaging.



**Figure 32: Selected area diffraction (SAD) pattern in the lab.-made alloy in condition 2 of precipitates (a) that were indexed as  $\beta''$  (b), camera-length 300mm.**

Figure 32 shows the results of selected area diffraction (a) and the indexing of the pattern (b). Based on the indexing and the morphology the precipitates were identified as  $\beta''$ . Images were also taken at grain boundaries. Figure 33 shows precipitate-free zone with a thickness of 20nm around the grain boundaries.

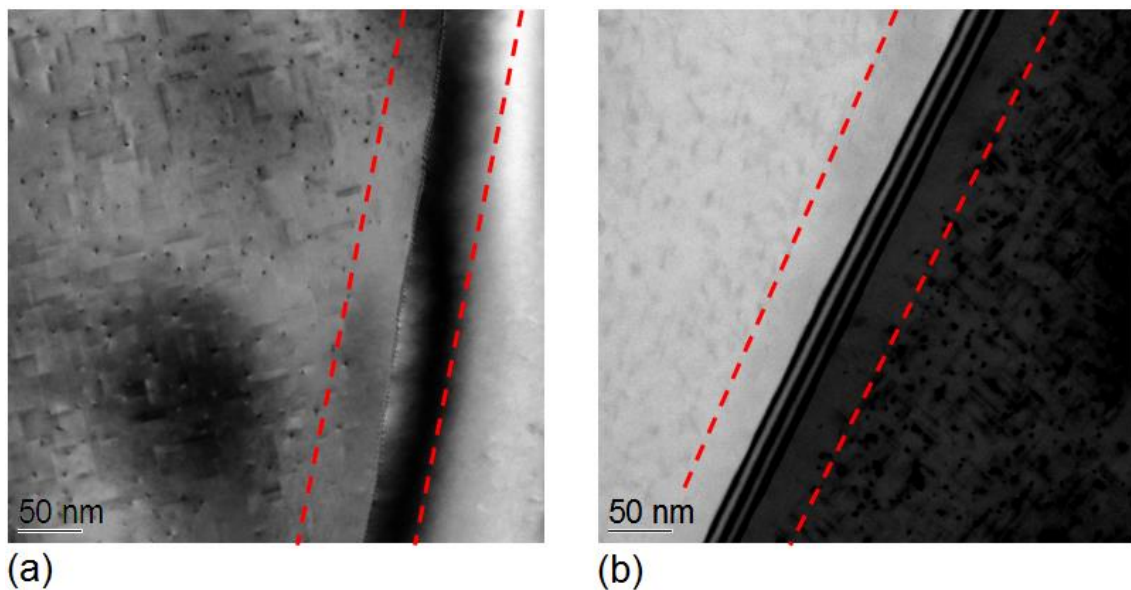


**Figure 33: Brightfield TEM-image along [001] of lab.-made (a) and ind. material (b) at condition 2 after 18h in industrial heat treatment showing precipitate-free zone (PFZ) at grain boundaries, marked with dashed lines.**

### 5.4.3 TEM – condition 3

Same investigations as in condition 2 were performed for condition 3. Figure 34 shows the TEM image of the laboratory-made and the industrial alloy. Again, 20nm long needle-shaped precipitates are visible in both alloys, which are orientated along  $\{100\}$  directions of the aluminium-crystal lattice. SAD patterns again identified the precipitates as  $\beta''$ . PFZ at grain boundaries were observed, which is shown in Figure 35

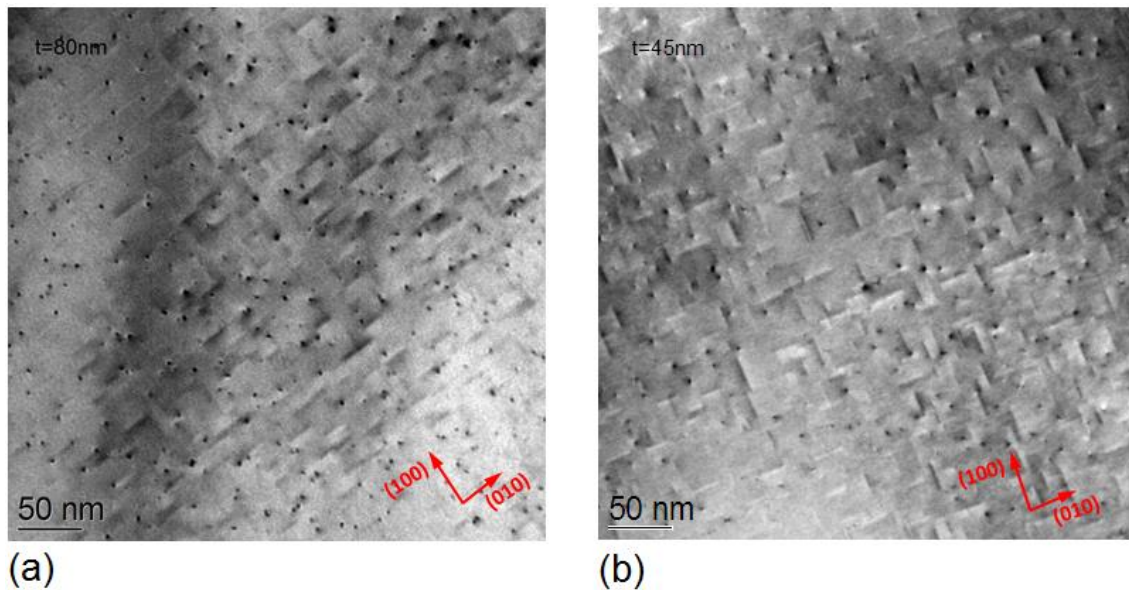


**Figure 34: Brightfield TEM-image of lab.-made (a) and ind. material (b) at condition 3 at the end of industrial heat treatment showing  $\beta''$  precipitates orientated along  $\{001\}$  directions.**

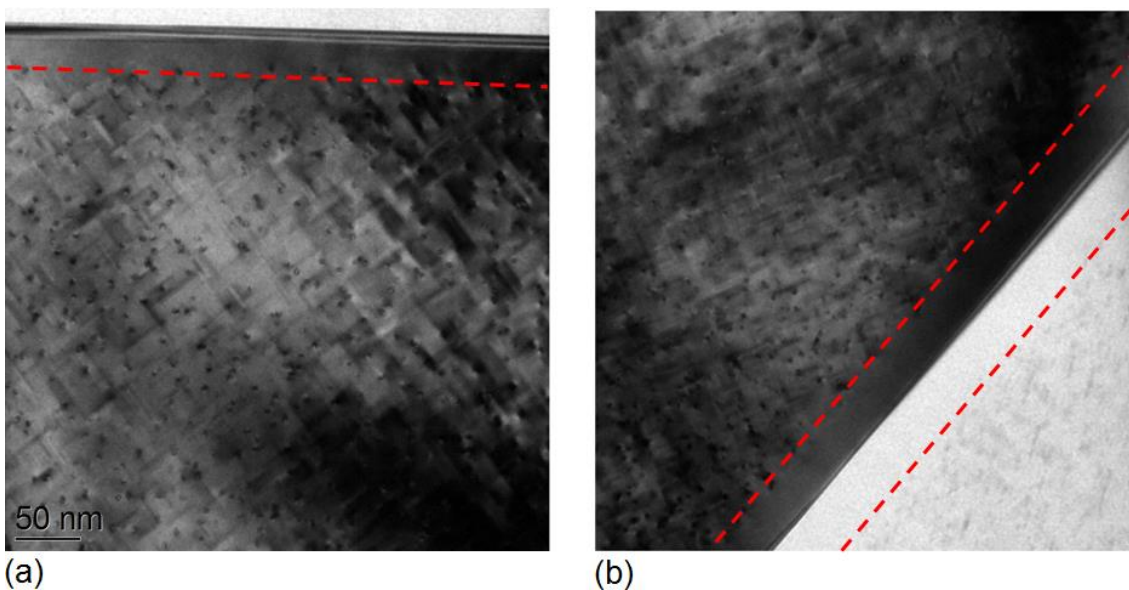


**Figure 35: Brightfield TEM-image along  $[001]$  of lab.-made (a) and ind. material (b) at condition 3 at the end of industrial heat treatment showing precipitate-free zone (PFZ) at grain boundaries, marked with dashed lines.**

#### 5.4.4 Evolution of precipitate size and number density

Precipitates were observed in both materials in condition 2 and condition 3. This makes a comparison of both alloys from the view point of precipitate size and number density possible. Also the evolution throughout the industrial heat treatment of these precipitate parameters can be investigated. The measurement of the size is rather simple. A proper software makes it possible to measure the elongation of precipitates that lie in the (001) plane. Thereby, the length of the precipitates can be determined. The diameter can also be measured in a similar way, by measuring the size of the spherical cross-sections of the precipitates which are orientated in [001] direction. For the identification of the number densities, some assumptions must be made. The precipitates in the (001) plane give a rather low contrast, which means that a counting of these precipitates can lead to failures, because maybe not all the present precipitates are visible in the TEM image. Furthermore, the diameter of the precipitates is low compared to the thickness of the samples, which is between 50 to 80nm. This means that several layers of precipitates can be present in the sample without being noticed, because of a lack in contrast. A better way is the counting of precipitates orientated along [001]. The assumption is made, that these precipitates give enough contrast so that every precipitate in the investigated area can be identified. The number of the precipitates in [001] direction in a specific area is then multiplied by 3, to get the number of all precipitates in the investigated area. This is legal, because the precipitates are all orientated only along the three axis of the crystal lattice. After that, the counted precipitates are then related to the volume, which can be calculated by multiplying the investigated area with the thickness of the sample. By changing the units to SI-units, the number density can be specified in particles per  $\text{m}^3$ . Results are shown in Table 5.

**Table 5: Number density, particle-size of precipitates and width of precipitate-free zones of both alloys at different conditions during industrial heat treatment.**

sample-ID/condition	number density [ $\text{m}^{-3}$ ]	size [nm]	PFZ [nm]
lab.-pure / 1	-	-	-
lab.-pure / 2	$1 \cdot 10^{21}$	$18 \pm 3$	$21 \pm 1$
lab.-pure / 3	$5 \cdot 10^{22}$	$20 \pm 3$	$34 \pm 2$
AA6016 / 1	-	-	-
AA6016 / 2	$1 \cdot 10^{23}$	$16 \pm 3$	$27 \pm 1$
AA6016 / 3	$1 \cdot 10^{23}$	$16 \pm 2$	$31 \pm 1$



---

## 6 Discussion

The results shown in section 5 make a comparison of the aging behavior of both alloys possible.

### 6.1 Metallography

Main result of the metallographic investigations is the big difference in grain size between the industrial AA6016 and the laboratory-made alloy. The grain size of the industrial material is approximately 4 times smaller than the grain size of the pure ternary alloy.

The main reason for this is the absence of grain refining elements, such as titanium and the amount of dispersoids available in the industrial material. Another contributing reason for this could be a difference in casting parameters, as shown in section 3.2.1. This is very unlikely, because the used Opticast technology during casting of the laboratory-made alloy provides nearly the same casting conditions. Another possibility is a high difference in the rolling parameters, which could not be proved because no detailed information about rolling of the pure ternary alloy was available.

Compared to the micrographs in Figure 9 it becomes clear, that the material must have recrystallized during the solution heat treatment. This can also be proven when comparing the results with figures given in the reference [9].

### 6.2 Comparison of the precipitation kinetics

Figure 36 shows the DSC signals which were recorded during the DSC investigations of both alloys. By comparing the obtained results with literature [29]-[33], the peaks were identified and are shown in Figure 36.

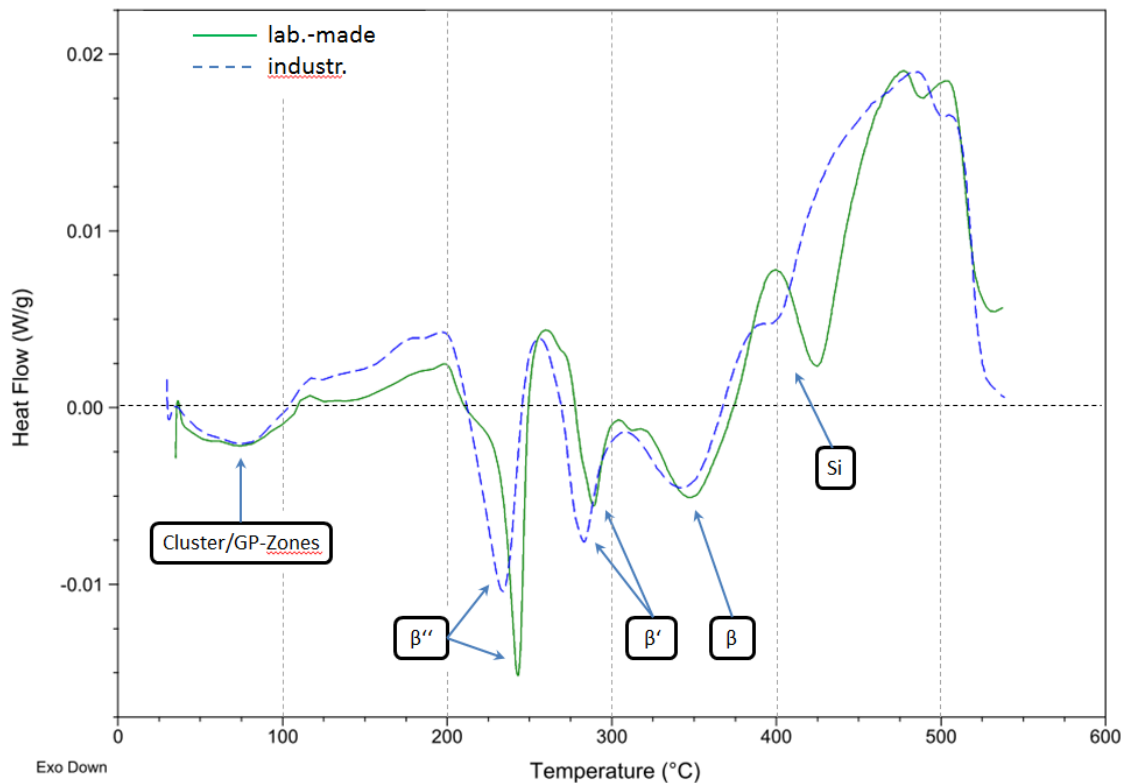


**Figure 36: Identification of precipitate-type in the DSC plot performed with a heating rate of 5K/min for the laboratory-made, as well as the industrial material.**

The first exothermic peak between room temperature and 100°C contributes to the formation of early stages of precipitation e.g. clusters, co-clusters and GP-zones. They are dissolved with increasing temperature, which can be seen via the endothermic peak between 100°C and 210°C. Following the precipitation sequence of Al-Mg-Si wrought alloys, the exothermic peaks around 230°C contribute to the formation of  $\beta''$  precipitates, followed by the endothermic dissolution peak. Next step is the formation of  $\beta'$  precipitates at approximately 280°C. One should keep in mind that also other phases can form parallel to  $\beta'$ , which was explained in section 3.6.2. In that case it is not possible to distinguish between those phases, because the formation of these phases creates only one exothermic peak in the DSC. This is followed by an endothermic peak, which contributes to the dissolution of these phases. One could disagree with this statement, because the DSC signals still shows a negative value around 310°C, which was defined as an exothermic reaction. This can be explained by the fact, that the signal shows the overall response of the system. That means that the endothermic reaction is maybe already overlapped by the exothermic reaction that is caused by the formation of stable  $\beta$  precipitates which is located around

350°C. This also occurs for the peaks that are located around 400°C. The values are all positive which shows an endothermic reaction, but the peak that decreases the absolute value of the signal is a sign for a superposition with an exothermic reaction. The exothermic reaction at this temperature corresponds to the formation of silicon precipitates. The large endothermic peak at the end of the signal corresponds to the dissolution of all phases that were formed during the precipitation sequence.

When comparing the signal of the industrial AA6016 with the laboratory-made pure alloy, two major differences can be recognized. The formation of precipitates happens at slightly lower temperatures in the industrial alloy. This difference always has a value of approximately 10°C. The effect can be explained by an energetic difference between the two alloys, caused by the higher amount of elements present in the industrial alloy. These elements act as nucleation spots for heterogeneous nucleation. As described in section 3.6.4, heterogeneous nucleation leads to a decrease in the critical energy  $G^*$  that must be overcome to make precipitation and growth possible. This is achieved by a decrease in volumetric misfit. Therefore, the formation of precipitates occurs already at lower temperatures. The second difference is the exothermic peak around 400°C that superimposes the large endothermic peak at the end of the DSC run. In case of the industrial AA6016 alloy only a saddle point is visible, while the laboratory-made alloy shows a significant exothermic reaction. Both, the saddle point and the exothermic peak may dedicate to the formation of pure silicon precipitates.

### **6.3 Differences in the Hardness evolution during industrial heat treatment**

As expected, the results in Figure 26 show an increase in hardness throughout the industrial aging heat treatment. The hardness of both alloys rises significantly between the as-quenched condition and the end of the heating ramp. A significant increase was observed also during the isothermal heat treatment step. During the second half of the isothermal step, the increase in hardness was not as significant as before.

The errors bars in the plot are quite large for both alloys and are also overlapping at some points, which means that the hardness evolution of both alloys is very similar. But there are still some tendencies observable. First of all the industrial AA6016 shows a higher hardness in the as-quenched situation than the laboratory-made pure alloy. Main cause is the lower grain size of the alloy, which contributes to the strength via grain boundary hardening (Hall–Petch strengthening). Second reason for this difference is the higher amount of dispersoids observed in TEM of industrial material. This difference between both alloys remains approximately constant until the middle of the isothermal section (condition 2) is reached. What can also be observed is the reduction of the hardness increase slope of the AA6016 alloy during the second half of the isothermal heat treatment step. Compared to this, the laboratory made alloy still increases its hardness until the end of the heat treatment. The hardness value of the laboratory-made pure alloy at condition 3 is questionable. This behavior was not expected and therefore results should be checked for reproducibility and if that is the case further investigations must be performed to find the reason for this behavior.

Except the hardness value for the laboratory-made alloy in condition 3, the results are in good accordance with literature [22], which can be seen when results are compared to the measurements in Figure 20. In that case the changes in hardness also were very small during an aging time of 6 to 12 hours.

It is shown, that the absence of accompanying elements does not affect the precipitation hardening significantly. This can be explained by the overall chemical composition of both alloys.

## **6.4 Comparison of TEM-results**

The results in Figure 27 show a difference in density of the dispersoid in both investigated alloys. It can be seen, that the amount of dispersoids in the industrial AA6016 alloy is significantly higher than in the laboratory-made alloy. This is caused by the much higher amount of accompanying elements present in the industrial material, which are able to form dispersoids. Thereby, also the chemical composition of these particles showed some differences. While the dispersoids in the laboratory-made alloy just consist of aluminium, silicon and

---

iron, the dispersoids in the industrial alloy also showed traces of other elements, such as manganese and copper. This is in good accordance with the overall chemical composition of the two alloys and literature [4].

The alloys did not show a significant precipitation in condition 1 in the TEM images. However, the hardness increased significantly when comparing the values of condition 1 with those of condition 0. This means, that clustering of atoms and early stages of precipitations such as GP-zones, must already have been occurred between these two steps, which caused this increase in hardness. This is also proved by the results of DSC investigations, because clusters and GP-Zones are formed at low temperatures that occur during the heating up step of the aging process. Obviously the maximum resolution of the used TEM is not high enough to contrast these particles. Condition 2 showed  $\beta''$  precipitates in both alloys, orientated in  $\{001\}$  along the aluminium matrix. They had a length of approximately 20nm and a diameter of 4nm, which is in good accordance to literature [22], [24]. The diffraction patterns identified the precipitates as  $\beta''$ . Condition 3 shows identical microstructure.

The precipitate-free zone (PFZ) adjacent to grain boundaries also appeared in both alloys. The reason for this is local depletion of solute concentration by heterogeneous nucleation on grain boundaries and also annihilation of vacancies at the grain boundaries, because excess-vacancies are energetically unfavorable and the grain boundaries are an efficient sink for them. This directly affects the diffusion in the area around the grain boundaries and leads to depression of precipitation, which contribute also to the precipitate-free zones [12].

The results concerning the number density and length of precipitates are given in Table 5. The number density of the laboratory-made alloy in condition 3 is smaller than the one in the industrial alloy, which implies a lower strength contribution of the precipitates in the laboratory alloys which should lead to lower strength in compare to industrial alloy. Hardness measurements show the reverse tendency. Therefore, further investigations should be performed to check the reproducibility of the measured hardness at condition 3 and if the result is reproducible, the reason should be clarified by a systematic detail study of the phenomenon.

An increase in number density between condition 2 and condition 3 of the laboratory-made alloy indicates increase of the hardness at condition 3 which is approved by experiment too.

The number density in the industrial alloy shows the same order throughout the industrial heat treatment. The length of the precipitates stays nearly constant. This approves the hardness experimental results concerning condition 2 and 3 of the industrial alloy.

The precipitate-free zones seem to grow throughout the heat treatment, but this cannot be proven by just investigating one grain boundary, because the boundaries could be cut under different angles which give different results. Therefore, the increase in size of the precipitate-free zones could be due to geometrical effect too.

---

## 7 Summary and Conclusion

The behavior of two alloys during aging was investigated. Metallography, differential scanning calorimetry (DSC), hardness tests and transmission electron microscopy (TEM) investigations were performed. Used materials are an industrial AA6016 aluminium wrought alloy and a laboratory-made pure alloy, which mainly consists of three main alloying elements aluminium, magnesium and silicon. Both materials showed nearly the same amount of basic alloying elements. Difference lied in the absence of accompanying elements, such as titanium, manganese and copper in the laboratory made pure alloy. The grain size of the two materials differs significantly. The laboratory-made alloy showed approximately four times larger grains than the industrial alloy, which is caused by the absence of grain refining elements, such as titanium and the higher amount of dispersoids. During DSC runs the industrial alloy showed formation of precipitates at slightly lower temperatures. This was explained by a higher amount of alloying elements, which act as nucleation spots for heterogeneous nucleation. This form of nucleation needs less energy compared to homogeneous nucleation, which explains the start of precipitation at lower temperatures.

The hardness of the industrial alloy after quenching is higher than the hardness of laboratory-made alloy. This difference will almost remain the same during the heat treatment and can be explained by considering the smaller grain size and higher number of dispersoids in the industrial alloy. But this tendency of higher hardness will be changed at the end of the heat treatment. This higher hardness of the laboratory-made alloy at the end was not expected and must be topic of further investigations.

The TEM investigations showed a higher number of dispersoids in the industrial alloy, due to higher amount of accompanying elements. Also the chemical composition of these dispersoids was investigated. In laboratory-made alloy they only included aluminium, silicon and iron, while the dispersoids in the industrial alloy also contains manganese and copper. In condition 2 and 3  $\beta''$  precipitates were detected in both alloys, showing almost the same morphology

and size throughout the industrial heat treatment. Also precipitate-free zones were detected around the grain boundaries in both alloys.

The results show, that the artificial aging process is not affected significantly by the absence of accompanying elements. The silicon which is bound in the primary phases, secondary phases and dispersoids is not affecting the precipitation of  $\beta''$  precipitates, because the overall composition of both alloys is approximately the same, although some silicon and magnesium is consumed for the formation of intermetallic phases. Main differences between the two alloys are the grain size and the composition and number of dispersoids.



## 8 References

- [1] D. . Eskin, *Physical Metallurgy of Direct Chill Casting of Aluminium Alloys*. Boca Raton, London, New York: CRC Press, 2008.
- [2] Bargel and Schulze, *Werkstoffkunde*, 11th ed. Berlin Heidelberg: Springer, 2012.
- [3] S. Wang, K. Matsuda, T. Kawabata, T. Yamazaki, and S. Ikeno, "Variation of age-hardening behavior of TM-addition Al–Mg–Si alloys," *J. Alloys Compd.*, vol. 509, no. 41, pp. 9876–9883, Oct. 2011.
- [4] N. C. W. Kuijpers, F. J. Venllocln, K. Vuik, and S. Van Der, "A Model of the  $\beta$ -AlFeSi to  $\alpha$ -Al(FeMn)Si transformation in Al-Mg-Si alloys," Delft University of Technology, 2004.
- [5] Y. Birol, "Formation and transformation of intermetallic particles in a strip-cast Al-0.8Fe-0.6Si alloy," *Zeitschrift für Met.*, vol. 89, no. 7, pp. 501–506.
- [6] S. N. Samaras and G. N. Haidemenopoulos, "Modelling of microsegregation and homogenization of 6061 extrudable Al-alloy," *J. Mater. Process. Technol.*, vol. 194, no. 1–3, pp. 63–73, Nov. 2007.
- [7] W. Kuijpers, I. Todd, and H. Kool, "Intermetallic phase transformation during homogenisation of 6xxx Al alloys," Delft University of Technology, 2000.
- [8] Y. Wu, J. Xiong, R. Lai, X. Zhang, and Z. Guo, "The microstructure evolution of an Al–Mg–Si–Mn–Cu–Ce alloy during homogenization," *J. Alloys Compd.*, vol. 475, no. 1–2, pp. 332–338, May 2009.
- [9] O. Engler, "Texture control by thermomechanical processing of AA6 xxx Al – Mg – Si sheet alloys for automotive applications — a review," vol. 336, pp. 249–262, 2002.
- [10] "Rolling Aluminum : From the Mine Through the Mill," The Aluminium Association Inc., 2007.
- [11] F. D. Fischer, J. Svoboda, F. Appel, and E. Kozeschnik, "Modeling of excess vacancy annihilation at different types of sinks," *Acta Mater.*, vol. 59, no. 9, pp. 3463–3472, May 2011.
- [12] M. Jacobs, "TALAT Lecture 1204 Precipitation Hardening," *Train. Alum. Appl. Technol.*, 1999.
- [13] L. Zhen and S. B. Kang, "DSC analyses of the precipitation behavior of two Al – Mg – Si alloys naturally aged for different times," no. December, pp. 349–353, 1998.

- 
- [14] S. Pogatscher, H. Antrekowitsch, H. Leitner, a. S. Sologubenko, and P. J. Uggowitzer, "Influence of the thermal route on the peak-aged microstructures in an Al–Mg–Si aluminum alloy," *Scr. Mater.*, vol. 68, no. 2, pp. 158–161, Jan. 2013.
  - [15] J. Banhart, C. S. T. Chang, Z. Liang, N. Wanderka, M. D. H. Lay, and A. J. Hill, "Natural Aging in Al–Mg–Si Alloys - A Process of Unexpected Complexity," *Adv. Eng. Mater.*, vol. 12, no. 7, pp. 559–571, Jul. 2010.
  - [16] C. Wolverton, "Solute–vacancy binding in aluminum," *Acta Mater.*, vol. 55, no. 17, pp. 5867–5872, Oct. 2007.
  - [17] S. Pogatscher, H. Antrekowitsch, H. Leitner, D. Pöschmann, Z. L. Zhang, and P. J. Uggowitzer, "Influence of interrupted quenching on artificial aging of Al–Mg–Si alloys," *Acta Mater.*, vol. 60, no. 11, pp. 4496–4505, Jun. 2012.
  - [18] E. Povoden-Karadeniz, P. Lang, P. Warczok, A. Falahati, W. Jun, and E. Kozeschnik, "CALPHAD modeling of metastable phases in the Al–Mg–Si system," *Calphad*, pp. 1–11, May 2013.
  - [19] E. Ozawa and H. Kimura, "Excess vacancies and the nucleation of precipitates in aluminium-silicon alloys," *Acta Met.*, vol. 18, pp. 995–1004, 1970.
  - [20] G. A. Edwards, K. Stiller, G. L. Dunlop, and M. J. Couper, "The precipitation sequence in Al–Mg–Si alloys," *Acta Mater.*, vol. 46, no. 11, pp. 3893–3904, Jul. 1998.
  - [21] G. D. Preston, "The Diffraction of X-Rays by Age-Hardening Aluminium Copper Alloys," *Proc. R. Soc. A Math. Phys. Eng. Sci.*, vol. 167, no. 931, pp. 526–538, Sep. 1938.
  - [22] N. Wanderka, R. Schiffmann, and J. Banhart, "Characterization of precipitates in aluminium-based alloy AW 6016," *Surf. Interface Anal.*, vol. 39, pp. 221–226, 2007.
  - [23] S. K. Son, S. Matsumura, K. Fukui, and M. Takeda, "The compositions of metastable phase precipitates observed at peak hardness condition in an Al–Mg–Si alloy," *J. Alloys Compd.*, vol. 509, no. 2, pp. 241–245, Jan. 2011.
  - [24] H. K. Hasting, W. Lefebvre, C. Marioara, J. C. Walmsley, S. Andersen, R. Holmestad, and F. Danoix, "Comparative study of the  $\beta'$ -phase in a 6xxx Al alloy by 3DAP and HRTEM," *Surf. Interface Anal.*, vol. 39, pp. 189–194, 2007.
  - [25] R. Vissers, M. a. van Huis, J. Jansen, H. W. Zandbergen, C. D. Marioara, and S. J. Andersen, "The crystal structure of the  $\beta'$  phase in Al–Mg–Si alloys," *Acta Mater.*, vol. 55, no. 11, pp. 3815–3823, Jun. 2007.

- 
- [26] S. J. Andersen, C. D. Marioara, R. Vissers, a. Frøseth, and H. W. Zandbergen, "The structural relation between precipitates in Al–Mg–Si alloys, the Al-matrix and diamond silicon, with emphasis on the trigonal phase U1-MgAl<sub>2</sub>Si<sub>2</sub>," *Mater. Sci. Eng. A*, vol. 444, no. 1–2, pp. 157–169, Jan. 2007.
- [27] S. J. Andersen, C. D. Marioara, a. Frøseth, R. Vissers, and H. W. Zandbergen, "Crystal structure of the orthorhombic U2-Al<sub>4</sub>Mg<sub>4</sub>Si<sub>4</sub> precipitate in the Al–Mg–Si alloy system and its relation to the  $\beta'$  and  $\beta$ " phases," *Mater. Sci. Eng. A*, vol. 390, no. 1–2, pp. 127–138, Jan. 2005.
- [28] "Lecture Script 'Werkstoffprüfung 2 - 308.859'," TU Wien.
- [29] O. Nodin, "Computer simulation of volume changes during phase transformation," TU Wien, 2010.
- [30] L. Zhen and S. B. Kang, "DSC analyses of the precipitation behavior of two Al – Mg – Si alloys naturally aged for different times," no. December, pp. 349–353, 1998.
- [31] A. Gaber, a. M. Ali, K. Matsuda, T. Kawabata, T. Yamazaki, and S. Ikeno, "Study of the developed precipitates in Al–0.63Mg–0.37Si–0.5Cu(wt.%) alloy by using DSC and TEM techniques," *J. Alloys Compd.*, vol. 432, no. 1–2, pp. 149–155, Apr. 2007.
- [32] A. K. Gupta, D. J. Lloyd, and S. a. Court, "Precipitation hardening in Al–Mg–Si alloys with and without excess Si," *Mater. Sci. Eng. A*, vol. 316, no. 1–2, pp. 11–17, Nov. 2001.
- [33] A. K. Gupta, D. J. Lloyd, and S. A. Court, "Precipitation hardening processes in an Al-0.4%Mg-1.3%Si-0.25%Fe aluminium alloy," vol. 301, pp. 140–146, 2001.
- [34] E. Kozeschnik, *Modeling Solid-State Precipitation*, 1st ed. New York: Momentum Press, LLC, 2013, pp. 60–61.
- [35] B. Sonderegger and E. Kozeschnik, "Generalized Nearest-Neighbor Broken-Bond Analysis of Randomly Oriented Coherent Interfaces in Multicomponent Fcc and Bcc Structures," *Metall. Mater. Trans. A*, vol. 40, no. 3, pp. 499–510, Jan. 2009.
- [36] "Lecture Script 'Aushärtung von Aluminiumlegierungen'," Technische Universität Darmstadt.
- [37] S. Bargel, *Werkstoffkunde*, 11. Auflag. Berlin: Springer Vieweg, 2012.

## 9 List of figures

Figure 1: Process-steps in the production of 6xxx-series alloys. ....	4
Figure 2: DC casting methods; early methods (a), modern electromagnetic casting (b) [1]. ....	5
Figure 3: Effect of cooling rate on grain size (a) and dendrite arm spacing (b) of Al-Cu alloys [1]. .....	6
Figure 4: Influence of melt temperature on cast structure of an AA2024 alloy [1]. ....	7
Figure 5: Influence of accompanying elements on grain size of as-cast Al-alloys [1]. ....	7
Figure 6: Phase diagram of an Al-Mg-Si alloy containig 0.9% magnesium [1]. ....	8
Figure 7: SEM of primary $\alpha$ and $\beta$ phases in an Al-Fe-Si alloy containing also Cu and Mn [5]. .	10
Figure 8: $\beta$ to $\alpha$ transformation in AA6063 during homogenization at 565°C for 6h [7]. ....	11
Figure 9: Grain structure of AA6016 after casting and homogenization (a), homogenization and break-down mill (b) and after tandem hot rolling (c) [9]. ....	12
Figure 10: Temperature profile during solution heat treatment, quenching and artificial aging of aluminium alloys. ....	14
Figure 11: Commonly accepted precipitation sequence in Al-Mg-Si alloys during aging. ....	15
Figure 12: Needle shaped $\beta''$ precipitates in an Al-Mg-Si alloy, along $\langle 001 \rangle$ zone axis [24]. ....	16
Figure 13: Scheme of a heat flux-DSC showing position of a sample and a reference material within the measurement cell [28]. ....	18
Figure 14: DSC plot of a AA6016 alloy directly after solution heat treatment (T4) measured with a heating rate of 5K/min [29]. ....	19
Figure 15: Free energy of cluster formation plotted over precipitate radius, explaining the critical nucleation radius and the energy barrier for precipitation [34]. ....	21
Figure 16: Coherency of precipitates with the surrounding matrix; complete coherency without (a) and with volumetric missfit (b); semi-coherent (c) and incoherent (d) precipitates [34]. ....	23
Figure 17: Shear mechanism on a precipitate during dislocation movement [36]. ....	23
Figure 18: Orowan mechanism; Dislocations pile up at precipitates and then pass by, leaving a dislocation loop around the precipitate [37]. ....	24
Figure 19: Hardness values during non-isothermal heat treatment with a heating rate of 10K/s in an Al-0.4%Mg-1.3%Si-0.25%Fe alloy [33]. ....	25
Figure 20: Hardness as a function of annealing time at various isothermal temperatures in AA6016 [22]. ....	25
Figure 21: Opticast sample (a) and the used laboratory-made pure alloy after rolling (b). ....	27
Figure 22: Heat treatment sequence for DSC measurements. ....	29
Figure 23: Industrial heat treatment process; numbers 1-4 show specific points where investigations were performed. ....	30
Figure 24: Micrographs (100x) of laboratory-made alloy (a) and industrial AA6016 (b) in T4 condition, showing the effect of grain refining elements. ....	32
Figure 25: DSC plot of industrial (dashed) and laboratory-made pure (solid) material directly after solution heat treatment, measurement performed with 5K/min. ....	33

Figure 26: Hardness as function of annealing time through the industrial heat treatment for laboratory-made and industrial material.....	34
Figure 27: TEM bright field images of condition 1 after a 12h in industrial heat treatment; Small dispersoids at grain boundairies and in bulk material of lab.-made alloy (a); larger precipitates in bulk with pinned dislocations in AA6016 (b). ....	35
Figure 28: Dark-field image and EDAX analysis of AlFeSi-dispersoids in lab.-made alloy. ....	36
Figure 29: Dark field TEM-image and EDAX analysis of AlFeMnSi-dispersoids also containing small amounts of copper in AA6016. ....	37
Figure 30: Brightfield TEM-image of lab.-made (a) and ind. material (b) at condition 1 at the end of the heating ramp in industrial heat treatment, showing no precipitation.....	37
Figure 31: Brightfield TEM-image of lab.-made (a) and ind. material (b) at condition 2 after 18h in industrial heat treatment showing $\beta''$ precipitates orientated along $\{001\}$ directions. ....	38
Figure 32: Selected area diffraction (SAD) pattern in the lab.-made alloy in condition 2 of precipitates (a) that were indexed as $\beta''$ (b), camera-length 300mm. ....	39
Figure 33: Brightfield TEM-image along $[001]$ of lab.-made (a) and ind. material (b) at condition 2 after 18h in industrial heat treatment showing precipitate-free zone (PFZ) at grain boundaries, marked with dashed lines.....	39
Figure 34: Brightfield TEM-image of lab.-made (a) and ind. material (b) at condition 3 at the end of industrial heat treatment showing $\beta''$ precipitates orientated along $\{001\}$ directions. ....	40
Figure 35: Brightfield TEM-image along $[001]$ of lab.-made (a) and ind. material (b) at condition 3 at the end of industrial heat treatment showing precipitate-free zone (PFZ) at grain boundaries, marked with dashed lines.....	40
Figure 36: Identification of precipitate-type in the DSC plot performed with a heating rate of 5K/min for the laboratory-made, as well as the industrial material. ....	44